American Mineralogist, Volume 81, pages 1036–1056, 1996

Surface structural controls on pyrite oxidation kinetics: An XPS-UPS, STM, and modeling study

CARRICK M. EGGLESTON,[1,*] JEAN-JACQUES EHRHARDT,[2] AND WERNER STUMM[3]

[1]L-219, Earth Sciences Division, Lawrence Livermore National Laboratory, P.O. Box 808, Livermore, California 94550, U.S.A.
[2]Laboratoire de Chimie Physique pour l'Environnement, Université Mixte de Recherche–UMR 9992, CNRS–Université Henri Poincaré, Nancy I, France
[3]Institute for Environmental Science and Technology (EAWAG), Swiss Federal Institute of Technology, CH-8600 Dübendorf, Switzerland

ABSTRACT

X-ray and ultraviolet photoelectron spectroscopy (XPS and UPS, respectively) and scanning tunneling microscopy (STM) were used to observe the initial oxidation of pyrite surfaces in air. The results show the growth of oxide-like oxidation products, with minor contributions from sulfate. UPS shows a decrease in the density of electronic states in the uppermost valence band of pyrite, corresponding to oxidation of surface Fe^{2+}. This allows reliable interpretation of STM images, which show that initial surface oxidation of Fe^{2+} proceeds by growth of oxidized patches. The borders of oxidized patches contain small segments oriented in the ⟨110⟩ and ⟨100⟩ directions. STM of as-received pyrite cube surfaces, oxidized in air for years, also show the importance of the ⟨110⟩ crystallographic directions, on the surface, in controlling reaction progress.

A model in which oxidation probabilities for Fe^{2+} surface sites are proportional to the number of nearest-neighbor oxidized (Fe^{3+}) sites was tested using a Monte Carlo approach and reproduces the surface patterns observed in STM.

An oxidation mechanism consistent with the XPS, UPS, STM, and Monte Carlo results is proposed. The rate constant for electron transfer from surface-exposed pyrite Fe^{2+} to O_2 is small. Electron transfer is more rapid from pyrite Fe^{2+} to Fe^{3+} present on the surface as an oxidation product, such as in the patches we observed. Fe^{2+} in oxide is a better reductant than Fe^{2+} in pyrite, so electron transfer to O_2 from the oxide is also fast. However, this two-step mechanism is faster overall only if electron transfer to the surface oxide patches is irreversible (e.g., because of S_2 oxidation or electron hopping within the surface oxide patches). Cycling of Fe between the Fe^{2+} and Fe^{3+} forms, particularly along borders between oxidized and unoxidized areas, is thus a key feature of the pyrite oxidation mechanism. An understanding of the surface electronic and band structure aids definition of the redox potentials of electrons in various surface states. Rates of electron transfer from these states to O_2 are estimated using a kinetic theory of elementary heterogeneous electron transfer.

INTRODUCTION

Pyrite is the most common sulfide mineral at the Earth's surface and is a key agent of electron cycling in the near-surface environment. Weathering of pyrite is estimated at 36×10^{12} g/yr (Garrels et al. 1973), involving 0.02 moles of electrons per square meter of land-surface area (Wehrli 1990). This current often drives other processes, such as formation of acid mine drainage (Barton 1978), mobilization and redox cycling of metals in sediments from mining and other environments (Moore and Luoma 1990; Calmano et al. 1994; Nimick and Moore 1994), degradation of pollutants (Kriegman-King and Reinhard 1994), reduction of aqueous trace metal complexes to form ore deposits (Jean and Bancroft 1985; Bakken et al. 1989), and nutrient and metal cycling at oxic-anoxic boundaries on lake bottoms and in estuaries (Morse 1994). Pyrite oxidation is also important in technological applications ranging from hydrometallurgy (Buckley and Woods 1987; Karthe et al. 1993) to solar energy conversion (Ennaoui et al. 1986).

Geochemical understanding of pyrite oxidation is largely based on wet-chemical studies of overall rates and stoichiometries. Important oxidants (e.g., O_2 and Fe^{3+}) have been identified and widely applicable rate laws developed (e.g., Singer and Stumm 1970; Williamson and Rimstidt 1994). Reaction mechanisms are less well known. Predicting and controlling the environmental aspects of pyrite oxidation, such as the role of Fe^{2+} at pyrite

* Present address: Department of Geology and Geophysics, University of Wyoming, Laramie, Wyoming 82071-3006, U.S.A.

0003–004X/96/0910–1036$05.00

surfaces in the reductive degradation of organic pollutants (e.g., see Kriegman-King and Reinhard 1994; Matheson and Tratnyek 1994), requires a better understanding of pyrite oxidation mechanisms. Detailed studies of surface atomic and electronic structure during oxidation help to constrain proposed mechanisms in a way that wet-chemical approaches cannot.

For most processes controlled by surface reactions, many types of surface sites, each with a different structure and reactivity, may contribute to the overall reaction. Surface structure is a fundamental control on reactivity. Different sites have different structures because they occur on different crystallographic faces, because they are at step, kink, or other defect sites on an otherwise flat surface, and because several types of sites may exist on an ordered surface plane. A source of much controversy in studies of mineral-water reactions is the fact that surface structure and the ratio of "more active" to "less active" sites are usually unknown, are sensitive to sample preparation, and are not uniform from laboratory to laboratory. Knowledge of controls on the reactivity of particular pyrite surface sites would improve our ability to predict and model pyrite oxidation rates.

We used X-ray photoelectron spectroscopy (XPS), ultraviolet photoelectron spectroscopy (UPS), and scanning tunneling microscopy (STM) to characterize fresh and oxidized pyrite (001) surfaces to understand oxidation mechanisms better, with particular attention given to the role of Fe^{2+}-Fe^{3+} cycling at the pyrite surface (e.g., see Moses and Herman 1991) and to the relative reactivities of different surface sites. We oxidized pyrite in air, but because water adsorbs readily at room pressure, a thin film of water was present. The results show oxidation of Fe^{2+} and growth of an Fe^{3+}-(hydr)oxide product in patches on the surface. We show that such patterns of oxidation can be explained if Fe^{3+}-containing oxidation products influence oxidation of further structural Fe^{2+}.

Summary of overall oxidation stoichiometries

Lowson (1982) reviewed electrochemical and wet-chemical pyrite oxidation studies. Biegler and Swift (1979) concluded that in aqueous solution pyrite oxidizes by a combination of the half-reactions

$$FeS_2 + 8H_2O \rightarrow Fe^{3+} + 2SO_4^{2-} + 16H^+ + 15e^- \quad (1)$$

$$FeS_2 \rightarrow Fe^{3+} + 2S + 3e^- \quad (2)$$

for which the dominant pathway depends on Eh and pH; the sulfate route dominates under ambient conditions. At low pH, pyrite is oxidized by O_2 and Fe^{3+}_{aq} (McKibben and Barnes 1986; Moses et al. 1987; Moses and Herman 1991; Rimstidt and Newcomb 1993; Williamson and Rimstidt 1994) according to the stoichiometries

$$FeS_2 + {}^7/_2O_2 + H_2O \rightarrow Fe^{2+} + 2SO_4^{2-} + 2H^+ \quad (3)$$

$$FeS_2 + 14Fe^{3+} + 8H_2O \rightarrow 15Fe^{2+} + 2SO_4^{2-} + 16H^+. \quad (4)$$

In Equations 1 and 4, O in SO_4^{2-} comes from H_2O, but in Equation 3 it comes from O_2. Taylor et al. (1984a, 1984b) and Reedy et al. (1991) showed by isotopic labeling that Equations 1 and 4 more accurately describe the source of O in SO_4^{2-}.

McKibben and Barnes (1986) present a rate law,

$$R = -kM_{Fe^{3+}}^{0.58\pm0.1} M_{H^+}^{-0.50\pm0.1} \quad (5)$$

in which rate R is normalized to pyrite surface area and $k = 10^{-9.74}$ mol/(cm^2·min) (30 °C). Rimstidt and Newcomb (1993), using several reactors and data analyses, obtained results in accord with Equation 5 for Fe^{3+} dependence. Williamson and Rimstidt (1994) added to the database, compiled literature data, and produced rate laws as a function of P_{O_2}, pH, and $[Fe^{3+}_{aq}]$ (where brackets indicate concentration).

At near-neutral pH, high rates, and low Fe^{3+} solubility make pyrite oxidation studies difficult. Moses and Herman (1991) concluded that adsorbed Fe may act as a "conduit" between pyrite and dissolved O_2, with Fe^{3+} accepting electrons from pyrite and the resulting Fe^{2+} donating electrons to O_2. Several researchers have characterized unoxidized, air-oxidized, and solution-oxidized pyrite surfaces with the use of surface spectroscopies (e.g., Brion 1980; Buckley and Woods 1987; Karthe et al. 1993; Nesbitt and Muir 1994). Evidence was found for the formation of Fe^{3+} oxyhydroxides of uncertain structure and the formation of basic iron sulfates. If oxidation products are not transported away from the surface (e.g., in air or in near-neutral pH solutions), solids can accumulate. These results, together with those of Moses and Herman (1991), focus attention on the role of oxidation products in electron transfer.

Experimental methods

Pyrite

Cubes (1 cm^3) were obtained at a mineral show (unknown locality) and fractured in air. For STM, the flattest possible surfaces are needed. We grooved the pyrite cubes with a diamond stylus and split the cubes by tapping on a blade in the groove. This produced rough surfaces, but small regions (1 mm^2 or less) were found nearly parallel to (001). We imaged only the flattest surfaces in detail. No attempt was made to control humidity or temperature exactly (laboratory temperature was 21 ± 1.5 °C).

Scanning tunneling microscopy

STM is based on tunneling currents between the sample and an atomically sharp metal tip rastered across the surface. The principles of STM and its use in mineralogy are discussed in Eggleston (1994). We used tungsten tips. Specific imaging conditions are given in the figure captions. All imaging was performed in air. The flatness of surfaces is important in STM. If the sample surface is not flat, tip and sample shapes become convoluted, complicating interpretation. Pyrite does not cleave, so obtaining

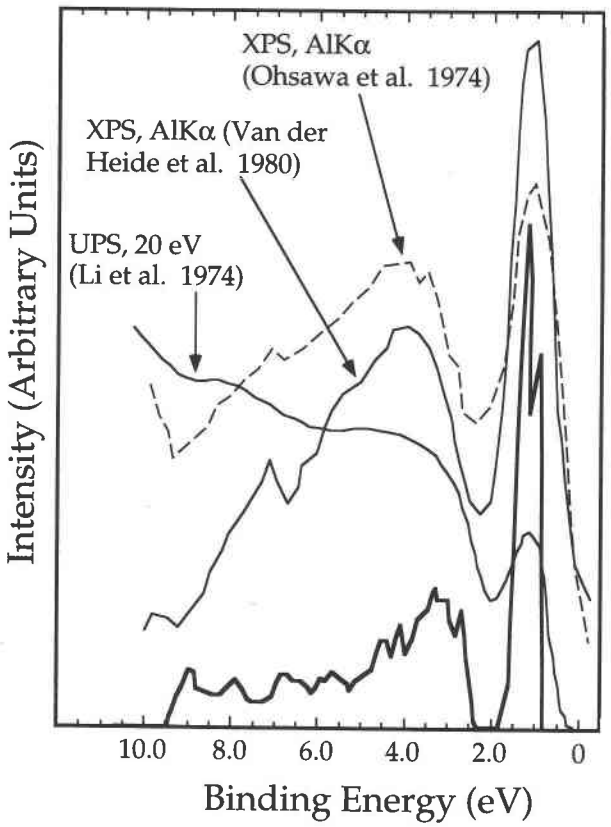

FIGURE 1. Pyrite valence-band electronic structure. Because the band energies are referenced to the vacuum level, and XPS and UPS binding energies are referenced to the Fermi level of the solid, the position of the calculated density of states (heavy line) was shifted to correspond with the experimental data. The density-of-states calculation does not consider photoionization probabilities, so the relative sizes of peaks cannot be compared. Differences in the UPS and XPS data are due to different photoionization probabilities for the different light energies. Differing relative intensities in the XPS data could be the result of small amounts of surface contamination. Spectra were digitized and replotted from the original papers.

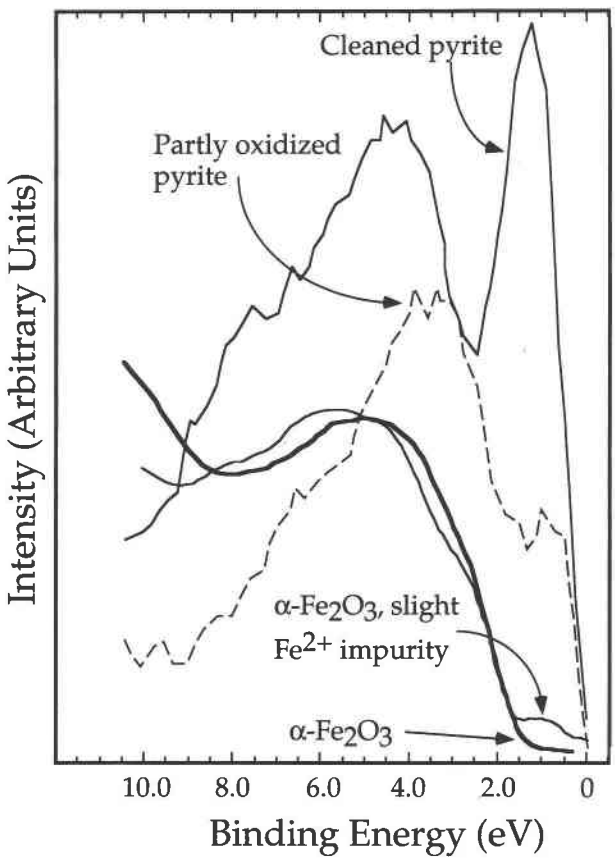

FIGURE 2. Comparison of valence-band photoemission spectra for cleaned pyrite (Ennaoui et al. 1986), pyrite supporting a residue of oxidation products (dashed line; Ennaoui et al. 1986), hematite (α-Fe_2O_3) with a slight Fe^{2+} impurity (Kurtz and Henrich 1987), and relatively pure hematite (heavy line; Hendewerk et al. 1986). The density of electronic states at the top of the valence band (0–1.5 eV binding energy) should decrease with oxidation progress. These data were digitized and replotted from the original publications.

flat surfaces was a problem. We therefore show the flatness of our surfaces in several figures.

STM studies of sulfides (Parkinson 1990; Eggleston and Hochella 1991, 1994) suggest that STM can affect the oxidation process. The reasons for this are probably electrochemical, but physical erosion of the surface by the tip is possible. Here, because oxidation is slow, we avoided this problem by imaging our samples only for brief periods after fracture and after oxidation. We could not image the exact same area before and after oxidation but did image nearly the same area. The STM results agree with the UPS and XPS data, so we are confident that the STM results are not artifactual.

Photoelectron spectroscopy

Spectra were obtained with a VSW HA150 MCD electron energy analyzer. A nonmonochromatic Mg$K\alpha$ source was used for XPS. Energy resolution was 0.9 eV. Base pressure was 2×10^{-10} mbar. The energy scale was calibrated using the Au 4f 7/2 (84.1 eV) and Ag 3d 5/2 (368.2 eV) lines. Raw spectra were Fourier smoothed. An integral base line was drawn, and peaks were fitted with a Gaussian-Lorentzian peak shape. One sample was fractured in air and quickly inserted into the vacuum chamber. The total time elapsed between fracture and vacuum ($<1 \times 10^{-3}$ mbar) was 3 min. Given the slow oxidation rates for pyrite found in other studies (Buckley and Woods 1987; Karthe et al. 1993), the only consequence of this was some contaminant C and O on the surface. This sample was labeled "fresh." UV photoelectron spectra were collected in the same vacuum chamber with the use of an He UV lamp emitting 21.21 eV light. The energy resolution for UPS was 0.2 eV as judged on the Fermi edge of a gold sample. Photoelectrons were collected along the surface normal.

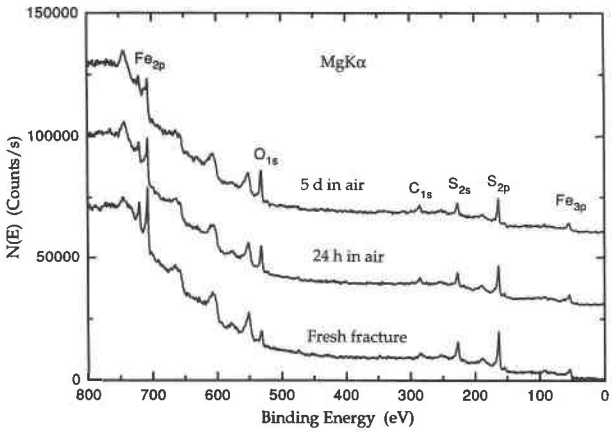

FIGURE 3. XPS survey spectra (one scan). The C 1s and O 1s peaks increase in relative intensity with air exposure, and the S and Fe peaks decrease. Auger electron and trace element peaks are not labeled.

Pyrite electronic structure

The pyrite structure can be derived from that of NaCl, with S_2 anions in the Cl position. Figure 1 summarizes the electronic structure of pyrite by comparing full nonempirical band-structure calculations (Bullett 1982) to spectroscopic data. Li et al. (1974) showed experimentally that the peak at the top of the valence band is primarily due to Fe 3d states, in agreement with the calculations. The top of the valence band (VB) is composed of occupied Fe 3d t_{2g} states, with S 3p states deeper in the VB (Bullett 1982). The conduction-band (CB) minimum is dominated by unoccupied Fe 3d e_g states. In STM, electrons tunnel either from the top of the VB to the tip or from the tip to the CB. Therefore, STM imaging at either polarity should give images dominated by Fe 3d states. Unless multiple-tip artifacts interfere with imaging, the centered square unit cell of the Fe^{2+} positions should be seen. There is some S 3p state density at the CB minimum, but our results are consistent with an Fe 3d-dominated CB. S atoms are present but do not have electronic states that the STM can "see" under the conditions used. Oxidation of Fe^{2+} alters the electronic structure by removing state density from the VB and CB edges (Fig. 2) and should be readily evident in STM imaging. Unoxidized Fe^{2+} should be seen as points of high tunneling current, and with oxidation the bright Fe^{2+} sites should "disappear" to form dark sites of low tunneling current.

RESULTS

Photoelectron spectroscopy

Our goal was not to conduct an exhaustive XPS study of pyrite oxidation but to obtain XPS, UPS, and STM results in parallel to be used in mutually constrained interpretations. Survey spectra were taken for fresh, 1 d, and 5 d air-oxidized surfaces (Fig. 3). The fresh surface had significant C and O contaminants. Some trends are apparent. With air exposure, Fe and S peaks decrease, whereas O and C peaks increase. C is a ubiquitous contaminant. O adsorbs to the surface and acts as an oxidant.

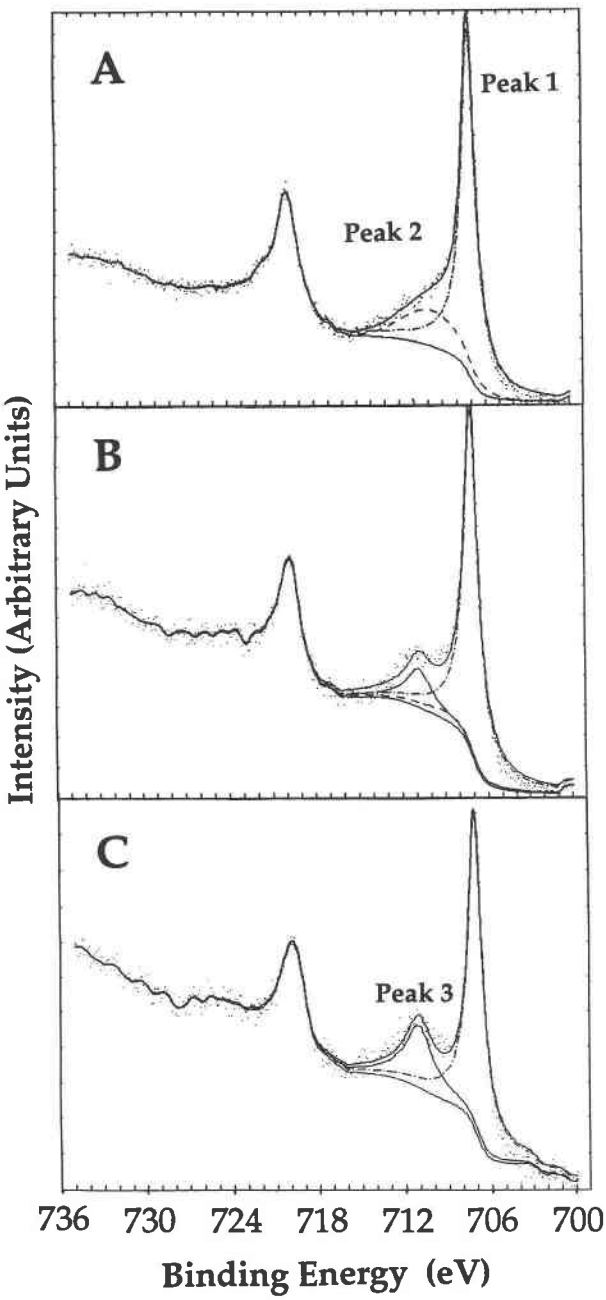

FIGURE 4. XPS Fe 2p spectra (ten scans). Only the Fe 2p 3/2 peak is fitted. Bottom solid line is background, top solid line is sum of background and fitted peaks. Peak 1 is the dot-dashed line; peak 2 is dashed line. Peak 3 is solid line in **B** and **C**. (**A**) Fresh fracture, (**B**) 1 d in air, (**C**) 5 d in air.

XPS spectra of the Fe 2p spin-orbit-split 3/2 and 1/2 peaks are found in Figure 4; only the 3/2 peak was fitted. The tail-off of intensity toward higher binding energy (BE) in the 709–716 eV range is common for pyrite, including those samples fractured in ultra-high vacuum (UHV) (Van

TABLE 1. Binding energies for Fe 2p ⅔ peaks in various model compounds in comparison with fitted peaks in Figure 5

Model compound	Binding energy (eV)	References
FeS	707.5	Pratt et al. (1994)
	707.5	Jones et al. (1992)
FeS_2	707.0	Nesbitt and Muir (1994)
	707.4	Brion (1980)
	707.4	Karthe et al. (1993)
	707.5	Ennaoui et al. (1986)
	707.0	Buckley and Woods (1987)
	707.0	Mycroft et al. (1990)
	706.7	Van der Heide et al. (1980)
FeO	709.5	McIntyre and Zetaruk (1977)
	709.6	Mills and Sullivan (1983)
Fe_2O_3	711.0	McIntyre and Zetaruk (1977)
	711.0	Harvey and Linton (1981)
	711.6	Mills and Sullivan (1983)
FeOOH	711.6	McIntyre and Zetaruk (1977)
	711.0	Harvey and Linton (1981)
$FeSO_4{\cdot}7H_2O$	711.3	Brion (1980)
$Fe_2(SO_4)_3$	713.5	Brion (1980)
$KFe(OH)_6(SO_4)_2$	712.2	Brion (1980)

der Heide et al. 1980; Mycroft et al. 1990; Karthe et al. 1993; Nesbitt and Muir 1994), and has been attributed partly to inelastically scattered electrons. Karthe et al. (1993) argued that multiplet splitting should not contribute intensity because low-spin Fe in $2p^63d^6$ S = 0 configuration leaves behind only a $2p^53d^6$ S = ½ ground state upon photoionization. However, the final state may not be a ground state. Gupta and Sen (1975) calculated multiplet splitting for free Fe^{2+} ions, and McIntyre and Zetaruk (1977), Pratt et al. (1994), and Nesbitt and Muir (1994) successfully fitted iron oxide, pyrite, and pyrrhotite photoemission data, respectively, using multiplet splitting. The degree of splitting may depend on defect structures at and near the surface, making it difficult to predict how much intensity is attributable to splitting. In any case, multiplet splitting does not account for all of the tail-off (Nesbitt and Muir 1994). Other possible contributors to tail-off of the main Fe 2p ⅔ peak in our spectra are as follows: (1) On the basis of the differences between pyrite and pyrrhotite spectra, Fe^{2+} in Fe^{2+}-S local coordination environments may have a slightly higher BE (0.3–0.5 eV) than in Fe^{2+}-S_2 environments in pyrite (Jones et al. 1992; Karthe et al. 1993). Such sites might occur on pyrite surfaces at defect sites, in some cases possibly produced by fracture. (2) Surface Fe^{2+}, after contact with air but before oxidation, is probably partly coordinated by O-containing species (e.g., O_2, OH^-, H_2O) adsorbed from air (note the O peak in the fresh-fracture spectrum in Fig. 4). The Fe 2p ⅔ peak for FeO occurs at 709.5 eV (McIntyre and Zetaruk 1977; Mills and Sullivan 1983). (3) Fe^{3+}-S environments might contribute to the 709–712 eV region (e.g., Pratt et al. 1994; Nesbitt and Muir 1994). Such sites could occur as defects resulting from fracture and as oxidation intermediates. (4) Fe^{3+}-O environments resulting from oxidation occur at about 711–712 eV.

Some of these contributors are defects that may be created by the damaging of pyrite surfaces (e.g., Fe^{3+}-S, Fe^{2+}-S, and Fe^{2+}-O environments) and may be consumed by oxidation (e.g., Fe^{2+}-O and Fe^{3+}-S environments). Ennaoui et al. (1986), Karthe et al. (1993), and Sasaki (1994) found that pretreatments that cause surface defects (such as grinding or Ar^+ bombardment) also increase the relative intensity of the high BE tail.

TABLE 2. Binding energy data (eV) for the fitted Fe 2p ⅔ peaks in this study (Fig. 5)

Fe 2p ⅔	Peak 1	Peak 2	Peak 3
Fresh fracture	707.1	709.6	—
1 d in air	707.1	709.0	710.8
5 d in air	707.1	—	711.9

In comparison with recent XPS studies of pyrite, we used a simplified peak-fitting approach. Rather than include many small peaks that constitute extra fitting parameters (even if they can be physically justified), particularly in the absence of independent information on the relative populations of possible contributing factors, we simply fitted the Fe 2p ⅔ spectra using a minimum number of peaks. Fe 2p ⅔ binding energies for various model compounds are listed in Table 1. The binding energies of peaks 1–3 in Figure 5 are given in Table 2. The results of the fitting of Fe 2p ⅔ peaks, along with other relative intensity data from this study, are given in Table 3. In Table 3, data series that show consistent trends are given in italics.

The fresh-surface spectrum (Fig. 4A) may be fitted using only two peaks: a narrow peak at 707.1 eV and a broad peak (peak 2 in Table 2, FWHM 4.8 eV) at 709.6 eV. After 1 d in air (Fig. 4B) three peaks are needed to fit the spectrum, but peak 2 can be largely replaced by a narrower peak (peak 3) at 711.1 eV characteristic of Fe^{3+} in oxides or oxyhydroxides (Table 1). After 5 d in air (Fig. 4C) peak 2 is no longer needed. The ratio of peak 3 to the total Fe signal increases from 0 to 0.28 (Table 3), consistent with the consumption of pyrite to form oxidation products (ferric oxide and oxyhydroxide, small amounts of ferric sulfate and basic sulfates such as jarosite). One interpretation of the loss of peak 2 with oxidation is that peak 2 intensity represents several surface defects of unknown structure, possibly including a few Fe^{3+}-O environments from incipient oxidation. Subsequent oxidation consumes some of these defects and forms more Fe^{3+}-O environments as products. Some of the defects, such as Fe^{2+}-O sites, may be important as initiators of the oxidation reaction. Indeed, Fe^{2+}-O environments have a binding energy of ~709.5 eV (Table 1), where peak 2 is centered.

The Fe 2p spectra are consistent with oxidation of Fe^{2+} and formation of ferric oxide or hydroxide-like oxidation products (e.g., see the Fe1/Σ Fe ratio in Table 3). The thickness T of the oxidation product layer can be estimated from

$$T = -\lambda_f \ln(I_c/I_{fr}) \quad (6)$$

TABLE 3. Trends in various peak ratios from XPS and UPS data, with oxidation progress

Signal ratio	Fresh fracture	1 d in air	5 d in air
Σ S/Σ Fe	0.46	0.64	0.60
Fe1/Σ Fe	*0.81*	*0.77*	*0.72*
Fe2/Σ Fe	*0.19*	*0.07*	—
Fe3/Σ Fe	—	*0.16*	*0.28*
S6/Σ Fe	—	0.11	0.05
XPS-VB/Σ S	0.93	0.81	0.88
XPS-VB/Σ Fe	0.43	0.52	0.53
UPS-VB/Σ S	*0.93*	*0.41*	*0.31*
UPS-VB/Σ Fe	*0.43*	*0.26*	*0.18*
UPS-VB/Σ Fe(1 + 2)	*0.42*	*0.31*	*0.25*

Note: Ratios listed are peak-intensity ratios only, not stoichiometric ratios. Σ S = total S signal (summed peaks); Σ Fe = total Fe signal (summed peaks); Fe1 = Fe, peak 1 (and so forth); XPS-VB = lowest binding energy peak in the XPS valence-band spectra; UPS-VB = lowest binding energy peak in the UPS valence-band spectra. Data that indicate consistent trends are shown in italics.

where λ_f is the attenuation length (related to the mean-free-path) of photoelectrons in the solid product layer, I_c is the intensity originating from the material covered by the layer, and I_{fr} is the intensity that would originate from a solid with no covering layer. For pyrite (see Seah and Dench 1979; Hochella 1988), λ_f is 10 ± 1 Å. We approximated I_{fr} by adding the intensities of peaks 1 and 3 (Fig. 4). The product layers are, assuming uniform layers and no concentration gradients, 1.9 and 3.3 Å thick for 1 and 5 d air exposure, respectively. A monolayer is 2.7 Å. One day of air exposure oxidizes less than a monolayer of Fe^{2+} sites.

XPS S 2p peaks have been analyzed extensively in other XPS studies of pyrite; we again chose to use a minimum number of peaks to fit the data. The main S 2p peak (peaks 2 and 3, Fig. 5) is split into ⅔ and ⅓ peaks, which dominate the spectrum. Following Karthe et al. (1993), peak 1 is attributed to an FeS-like environment; intensity in the region of peaks 4 and 5 is commonly attributed to polysulfides. Intensity in the 167.5–170 eV region (peak 6) increases with oxidation and has been attributed to a jarosite-like basic ferric sulfate (Karthe et al. 1993). Nesbitt and Muir (1994) concluded that surface Fe^{2+} oxidizes before disulfide; our results are consistent with this (e.g., compare the S6/ΣFe trend to the Fe3/ΣFe trend in Table 3).

The XPS-VB and UPS-VB spectra are of primary interest here because they can be directly related to STM results. Unlike core-level peaks, VB peaks reflect orbital mixing (bonding), so interpretation of VB peaks can be problematic. For pyrite, we are fortunate because the peak at the top of the VB is dominated by Fe 3d states (Fig. 1), and because C- and O-containing contaminants and oxidation precursors or products have little or no state density in this energy region (Fig. 2).

The XPS-VB spectrum of the fresh surface is in agreement with previous studies, both spectroscopic (Fig. 6A) and computational (Fig. 1). The peak at 0.8 eV is due to Fe 3d states of Fe^{2+} in pyrite (Fig. 2). The decrease in intensity of this peak (Fig. 6B), which we call the XPS-VB peak, is partly due to signal attenuation by overlying contaminant layers or oxidation products. There is little systematic change in the ratio of this peak to the total Fe 2p ⅔ or S 2p intensities (Table 3). The ratio of XPS-VB to total Fe 2p increases slightly, which is counterintuitive if the XPS-VB peak represents Fe^{2+} that is consumed by oxidation. Because the kinetic energy (KE) of VB photoelectrons ejected by 1253 eV Mg$K\alpha$ radiation is in the

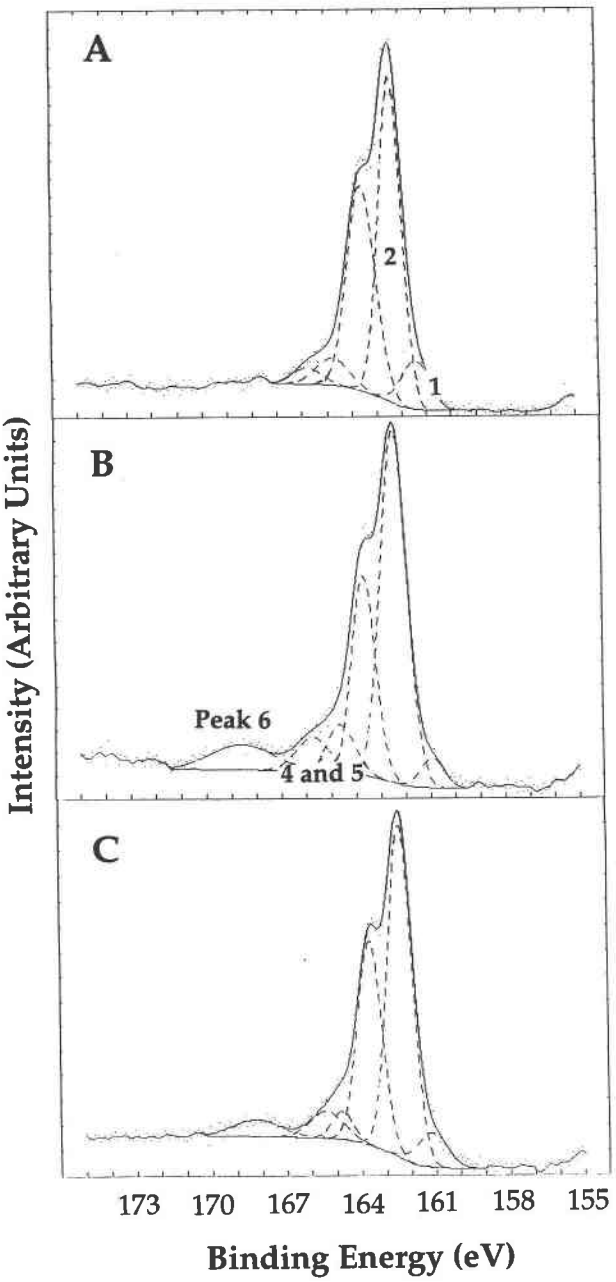

FIGURE 5. XPS S 2p spectra (eight scans). Fitted peaks are numbered in **A** and **B**. Bottom solid line is background, top solid line is sum of background and fitted peaks. (**A**) Fresh surface, (**B**) 1 d in air, (**C**) 5 d in air.

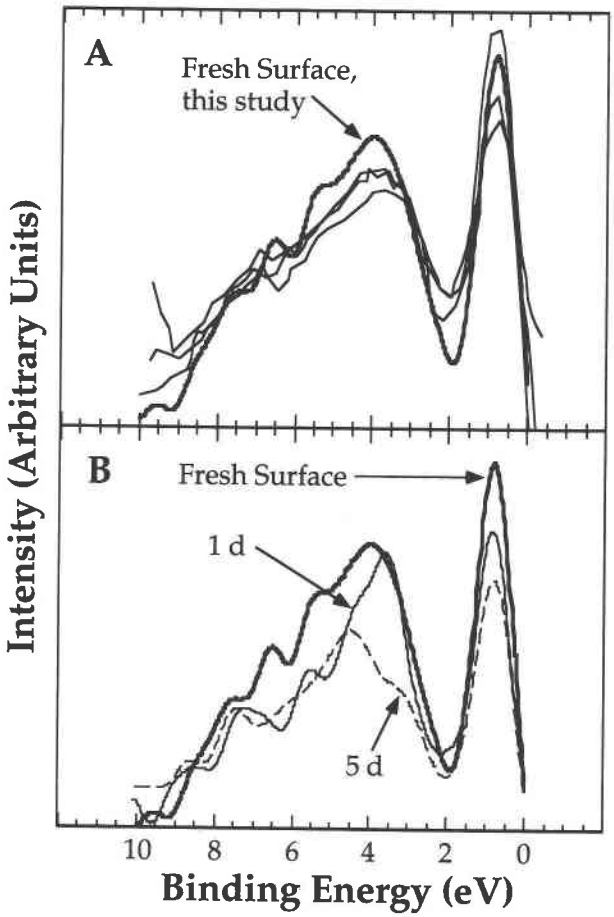

FIGURE 6. XPS valence-band spectra (ten scans). (A) Our spectrum for the fresh surface in comparison with spectra from Ohsawa et al. (1974), Van der Heide et al. (1980), and Ennaoui et al. (1986). (B) XPS-VB spectra for our fresh and air-exposed surfaces.

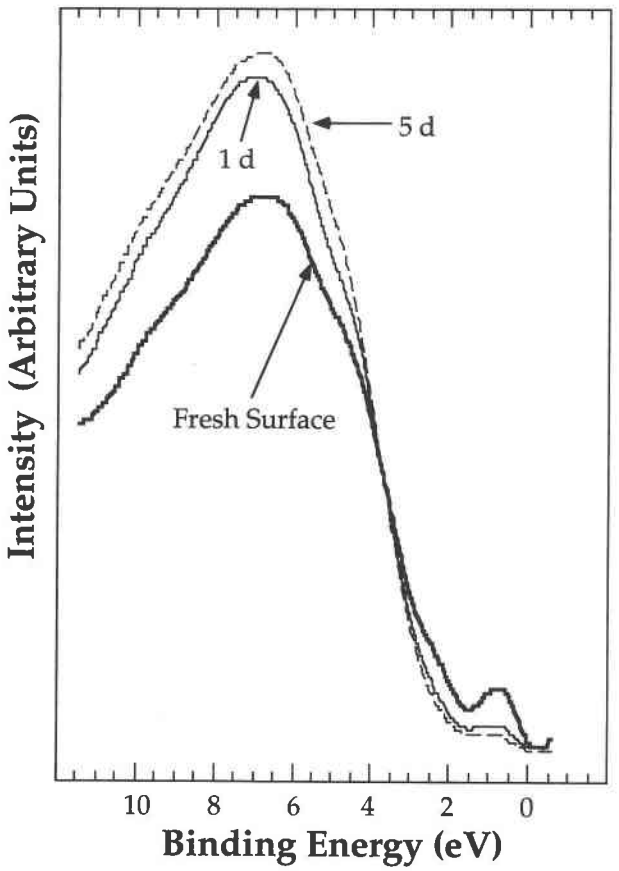

FIGURE 7. UPS valence-band spectra (four scans). The peak at the top of the VB decreases in intensity, whereas the intensity for BEs higher than 4.0 increases. States at the top of the VB are removed by oxidation; contaminants and oxidation products cause the increase of intensity deeper in the VB.

1230–1250 eV range, it is possible that their escape depth is larger than that of Fe 2p photoelectrons (KE ≈ 540 eV), making the XPS-VB spectra less surface sensitive than the core-level spectra; contaminants and oxidation products would attenuate the Fe 2p signal more than the VB signal, resulting in artifactual increases in the XPS-VB/Fe 2p ratio. Another possibility is that, because X-ray photoionization probabilities for VB states are small, small changes in photoionization probability with changes in local bonding environments may affect peak ratios.

The UPS-VB spectra are more useful (Fig. 7). The relative intensities are different from those of the XPS-VB spectra because of different photoionization probabilities for UV light. The 0.8 eV peak represents Fe 3d t_{2g} states of Fe^{2+} (see Fig. 2), and we call it the UPS-VB peak. The absolute and relative intensities of the UPS-VB peak decrease with air exposure, and the attenuation is directly related to loss of Fe^{2+} by oxidation and the appearance of Fe^{3+} in core-level spectra (Table 3). The UPS-VB peak intensity varies inversely with the Fe 2p intensity attributed to Fe^{3+}-oxide or oxyhydroxide (Fig. 8), as expected when consumption of one material is proportional to the growth of another material. The UPS-VB peak corresponds to electrons that the STM sees, and the loss of these states from the surface should be visible in STM images.

Scanning tunneling microscopy

Preparation of flat surfaces for STM was difficult. Microtopography images (100–600 nm on a side) were used to assess local flatness and to select areas for high-resolution imaging. However, it was necessary to obtain images quickly. The reason for haste is apparent in Figure 9. The areas that had been previously imaged appear rough when imaged again. The roughness was probably caused by STM-accelerated oxidation, although it could also have been caused by physical scouring of the surface by the STM tip (see Eggleston 1994).

Figure 10 shows the flattest surface we produced (the two images were obtained within minutes of fracture). There is clear evidence of a double (possibly triple) tip, which artifactually complicates microtopography near step edges. Surfaces rougher than those in Figures 9 and 10

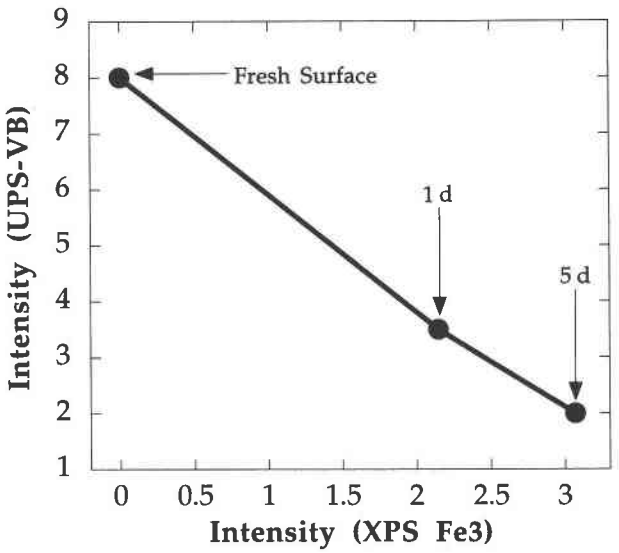

FIGURE 8. Negative correlation between the UPS-VB peak intensity and the intensity of peak 3 in Figure 5 (due to oxidized Fe). Peak intensities in arbitrary units.

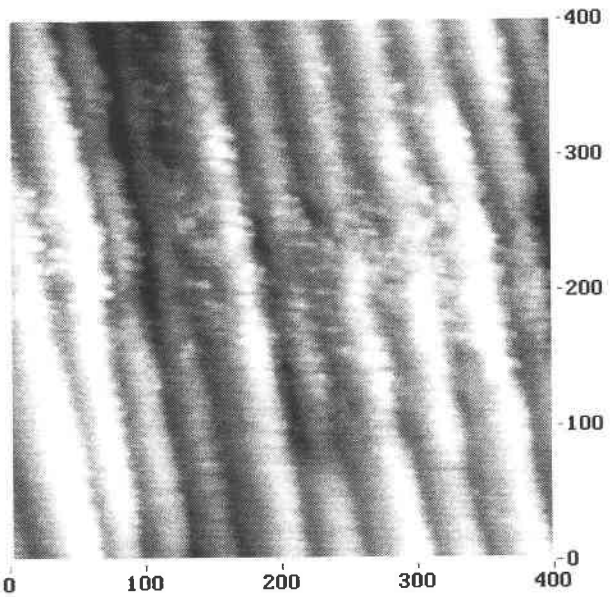

FIGURE 9. STM image of a pyrite fracture surface, nearly parallel to (001), 400 × 400 nm, after 5 min of imaging in several 150 × 150 nm areas in the center and center-right area. Numbered scales in nanometers. Conditions: 1.1 nA, 299.2 mV. Steps are ~1 nm high.

were impossible to interpret reliably because of the many multiple-tip artifacts that rough surfaces cause.

Fresh pyrite {001} surfaces, between steps, appear almost atomically flat (Fig. 11). In Figure 11A, two steps cross the image nearly vertically; the step on the left is a single molecular layer high, and the step on the right is two layers high. There is evidence of a double tip. The step edges exhibit a sawtooth pattern related to lineations at 45° to the step edges (i.e., in ⟨110⟩ directions). The root-mean-square (rms) roughness of the terrace alone (excluding the steps) is 0.018 nm, and the maximum roughness is about 0.06 nm. Much of this roughness was caused by a vibration artifact; the nonartifactual roughness of the surface is less than the above values suggest (Figs. 11B and 11C). The ⟨110⟩ lineations are less than a single atomic layer high and therefore cannot be steps but must represent local defects that affect electronic structure or work function.

The ⟨110⟩ lineations are probably related to twinning. Lowson (1982) cited "indistinct" cleavage along (100) and (111) twinning planes. A (111) plane intersecting the surface in Figure 11A would give lines as observed. Martello et al. (1994) examined the relationship between pyrite oxidation reactivity and stacking fault density, but the lineations we observed are not the same as their (010) stacking faults.

Figure 12A is an STM image of a slightly different area of the surface shown in Figure 11A, after 1 d of air exposure. The near-vertical trend of the step edges is still evident, but the terraces have greater topographic roughness, which is distributed over the surface differently than in Figure 11A. The rms and maximum roughnesses are 0.06 and 0.28 nm, respectively (Figs. 12B and 12C). Increased roughness is unequivocally due to a surface reaction because possible artifacts of STM were avoided. The patterns of roughness on the oxidized surfaces are instructive; in Figure 13, edges between dark and light areas parallel to ⟨110⟩ and ⟨100⟩ directions are marked.

Because of the many ⟨110⟩ lineation defects (Fig. 11A), it was difficult to find large areas for uninterrupted atomic-scale imaging of the terrace. Figures 14 and 15 are examples of high-resolution imaging of an unoxidized surface. In Figure 15B, a ⟨110⟩ lineation is seen as an unusually bright row of atoms next to an unusually dark row. This could have been caused by relaxation of atomic positions or by altered electronic structure. If the ⟨110⟩

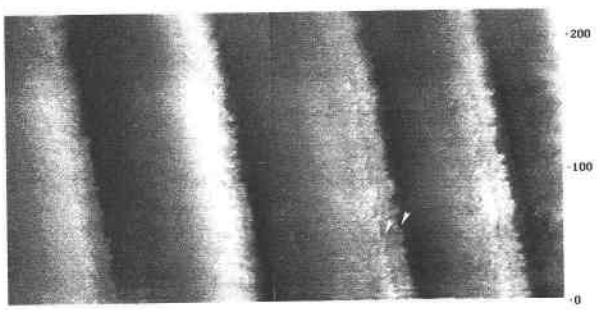

FIGURE 10. Two STM images of a fresh pyrite fracture surface, tiled together. White arrows indicate two images of the same step edge, the result of a double-tip artifact that manifests itself on all the steps. Total vertical relief in these images is 1.5 nm, and the steps are (after accounting for artifacts) about 1 nm high, or two unit cells. Numbered scales in nanometers. Conditions: 1.0 nA, 400.0 mV.

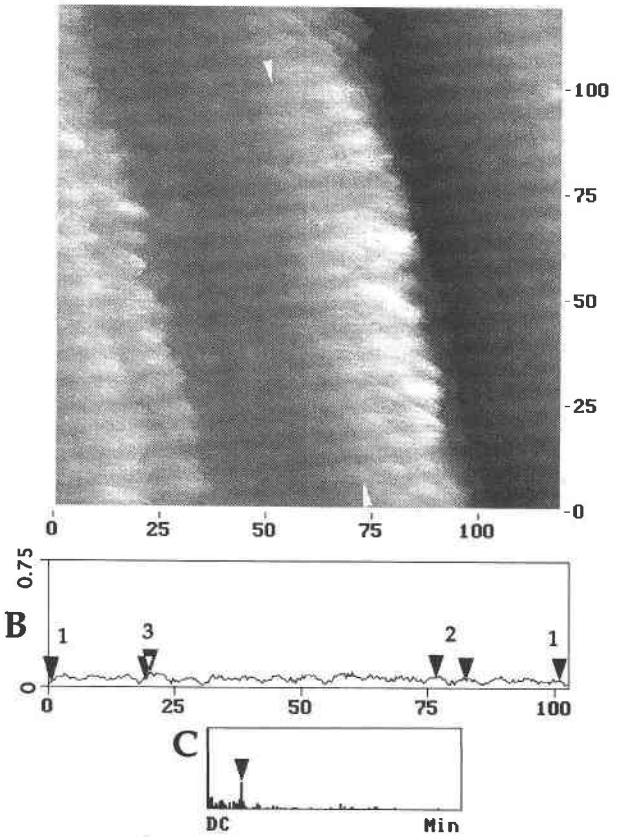

FIGURE 11. (A) Fresh pyrite fracture surface. The step on the right is 1 unit cell (5.4 Å) high. The periodic modulation, with wave crests running nearly perpendicular to the steps, is a vibration artifact. Conditions: 1.0 nA, −316.2 mV. (B) Cross section between white arrows in A. Root-mean-square roughness through the section is 0.018 nm. Arrows marked "1" are end points for the one-dimensional fast Fourier transform in C. Arrows marked "2" show the wavelength of the noise modulation seen in A (5.88 nm). Arrows marked "3" show an abrupt apparent elevation change across one of the 45° lineations in A; the apparent elevation difference is 0.38 Å (less than atomic dimensions). (C) One-dimensional fast Fourier transform of the elevation data in B. "DC" is the low-frequency limit (longest wavelength, the length of the cross section), and "Min" is the minimum wavelength (related to scan density, 512 lines per image). The peak marked with an arrow represents a wavelength of 5.87 nm, showing that the artifactual noise modulation is the only significant periodic feature in B; there is very little nonartifactual topography on the terraces. All numbered scales are in nanometers.

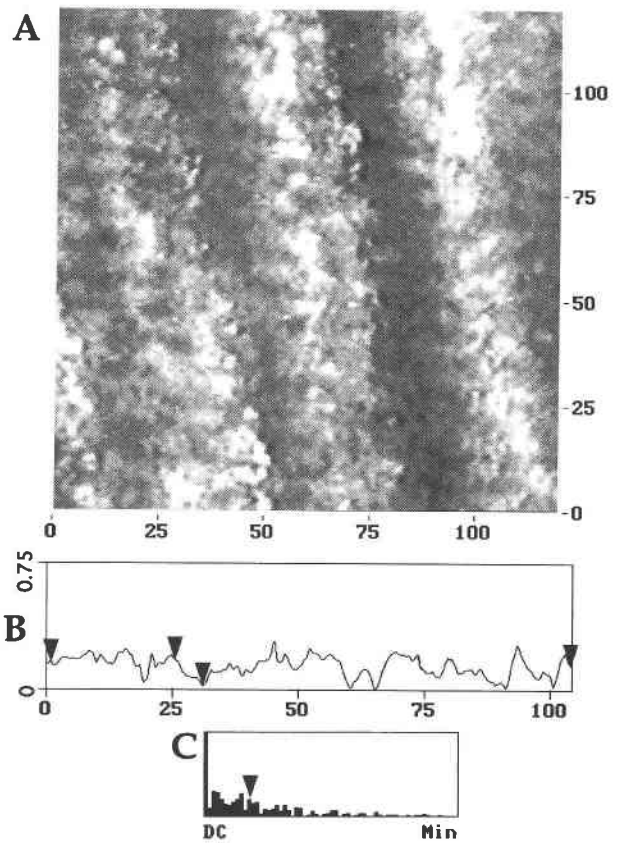

FIGURE 12. (A) Pyrite fracture surface after 1 d in air. Conditions: 1.0 nA, −40.0 mV. All scales in nanometers. (B) Cross section taken from a line near the left edge of A. Root-mean-square roughness is 0.059 nm, and the maximum roughness is 0.275 nm. The arrows at the ends of the cross section give the data range used in C, and the two arrows left of center show an elevation difference of 0.175 nm. (C) The frequency of the artifactual noise modulation, still barely visible in A, with a period of 5.87 nm, cannot be readily discerned in this one-dimensional fast Fourier transform of B. Labels are the same as for Figure 11C.

lineations represent twin planes intersecting the surface, the S_2 pairs may be oriented differently on opposite sides of the defect, leading to a local work-function difference that would be expressed in STM as an apparent topography difference (and that would imply an electric dipole across the defect).

One of the possible contributions to tail-off in the Fe 2p ⅔ XPS peaks (Fig. 4) is defects. Figure 11A shows that surface defects exist, with a frequency of about 0.15 defects/nm perpendicular to their orientation. Fe atoms have a frequency of 3.04 atoms/nm in this direction, giving a defect density of about 0.05 defects per surface Fe atom. Assuming that a defect affects only one atom where it crosses a line of atoms, this gives 5% of surface sites as defects, which is near the XPS detection limit. If we assume two atoms are affected where a defect crosses a line of atoms, and add defect sites at steps, 10–15% of surface sites would be affected by defects, which is in rough agreement with the XPS results for peak 2 in the Fe 2p ⅔ spectra (Table 3). If these defects contribute to the XPS spectra, the XPS results imply that defects as seen in Figure 15B should not be seen on oxidized surfaces. Indeed, as the results below indicate, the ⟨110⟩ lineations are not clearly evident on the oxidized surfaces.

Whenever atomic resolution was reliably obtained (Figs. 14 and 15), a centered square unit cell was observed, as

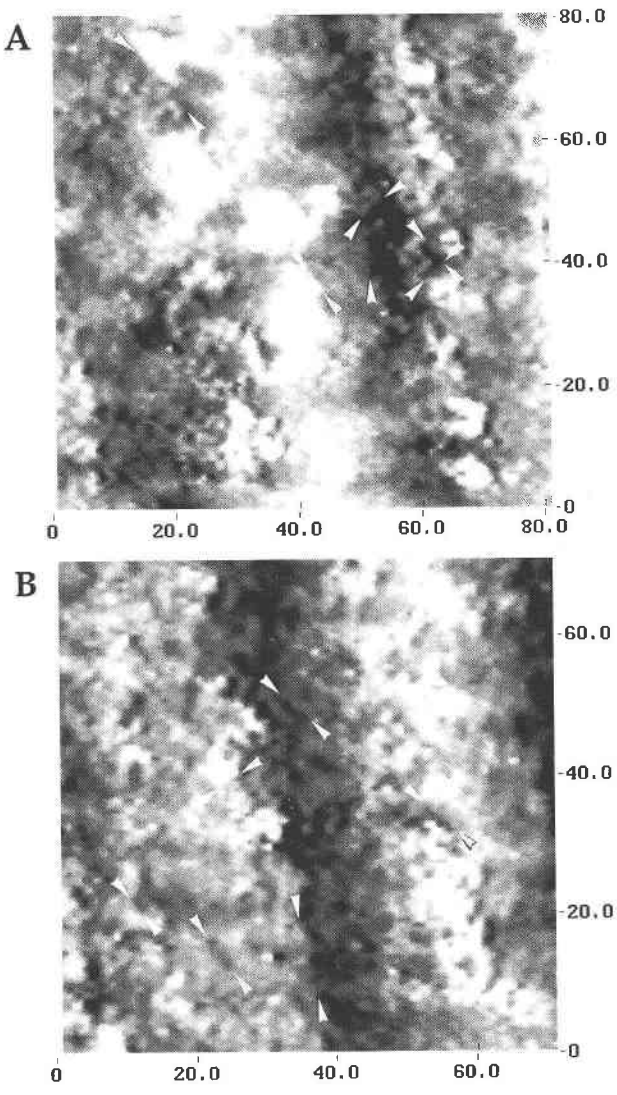

FIGURE 13. (A) Pyrite surface after exposure to laboratory air for 1 d (81.2 × 81.2 nm). (B) Slightly different area (71.4 × 71.4 nm) of the surface shown in A. In both images, arrows mark a few edges between light and dark areas that parallel ⟨110⟩ or ⟨100⟩. Conditions for both images: 1.0 nA, −40.0 mV. All scales in nanometers. Vertical relief is 1 nm.

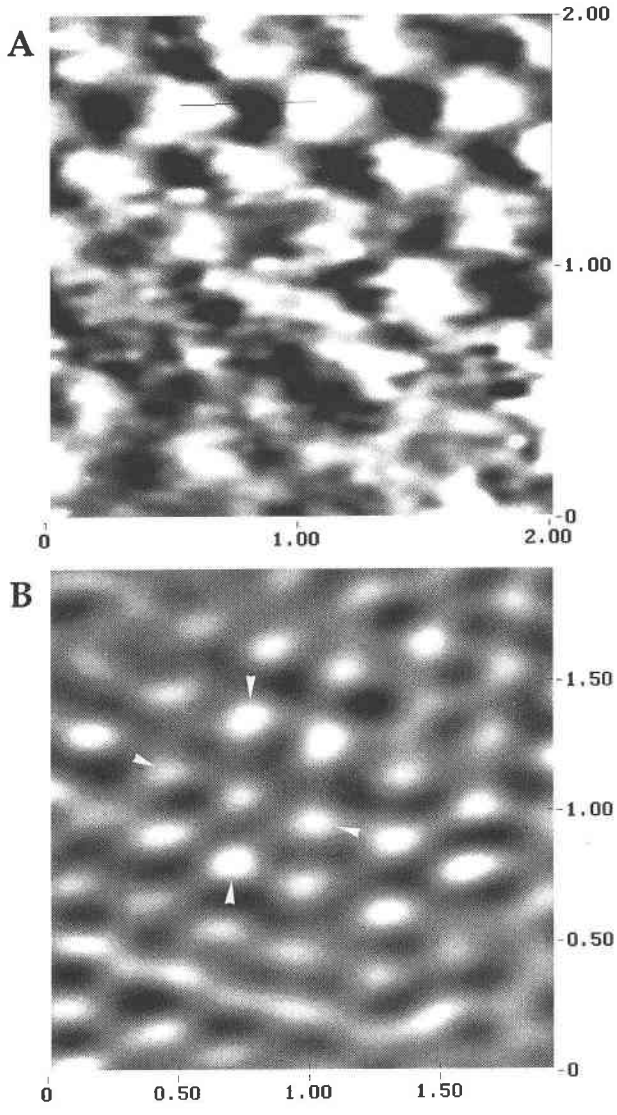

FIGURE 14. STM images of a fresh pyrite surface, showing occupied (VB) states. Both images were collected in constant-height mode (light = high current, dark = low current). Both images show a pattern of bright spots consistent with Fe positions in the square pyrite unit-cell face. Scales are in nanometers. (A) Conditions: 954.3 pA, −75.0 mV. The line marks a distance of 5.45 Å, in close agreement with the pyrite unit-cell edge of 5.42 Å. The sample was oriented with [100] and [010] nearly parallel to the edges of the image. This image was digitally low-pass filtered to remove high-frequency noise. (B) Conditions: 955.6 pA, −96.6 mV. The corners of a unit cell are marked with arrows. Sample was positioned with [100] and [010] oriented at about 45° to edges of the image. This image was Fourier-filtered to remove high-frequency noise.

expected from the Fe^{2+} substructure; it was also observed on pyrite imaged in oil (Eggleston and Hochella 1992) and is consistent with the top of the VB and the bottom of the CB, both being dominated by Fe 3d states (Bullett 1982).

The images in Figures 16 and 17 are from the same surface as shown in Figures 11A and 12, but after 26 h of exposure to air. Figure 16A is an image of a terrace between two parallel steps. Atomic-scale periodicity is visible, albeit noisy. There is an obvious double-tip artifact (repeated shapes are marked by pairs of white arrows). Despite these problems, some areas of the terrace clearly show the unoxidized structure of the pyrite surface, and other areas appear dark. These are the same dark areas seen in Figures 11A and 12. The overall elevation difference between the left and right edges is due to steps (oriented vertically) on the original fracture surface, whereas the dark patches within the terraces stem from postfracture oxidation. The surface is not complete-

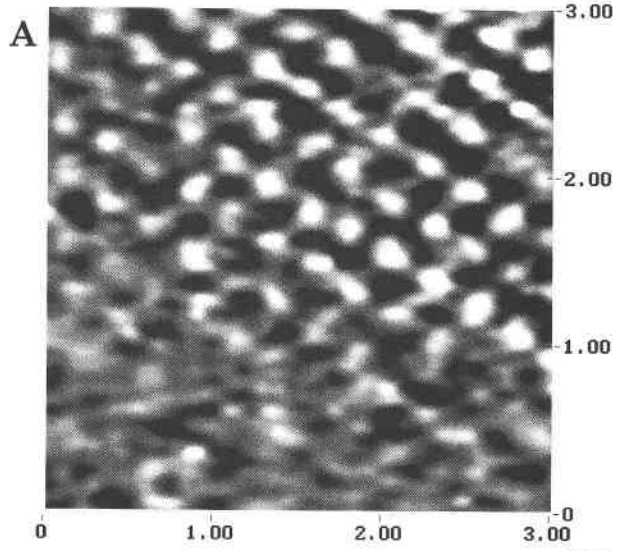

FIGURE 15. Constant-height STM images of a fresh pyrite surface, showing unoccupied (CB) states. Scales in nanometers. Both images were digitally filtered to remove high-frequency noise. The sample was oriented with [100] and [010] nearly parallel to the edges of the image. The images show a pattern consistent with Fe positions. **(A)** Conditions: 1.5 nA, 300.0 mV. **(B)** Conditions identical to those in A; one of the ⟨110⟩ defects (Fig. 11A) runs from upper left to lower right across the upper right corner.

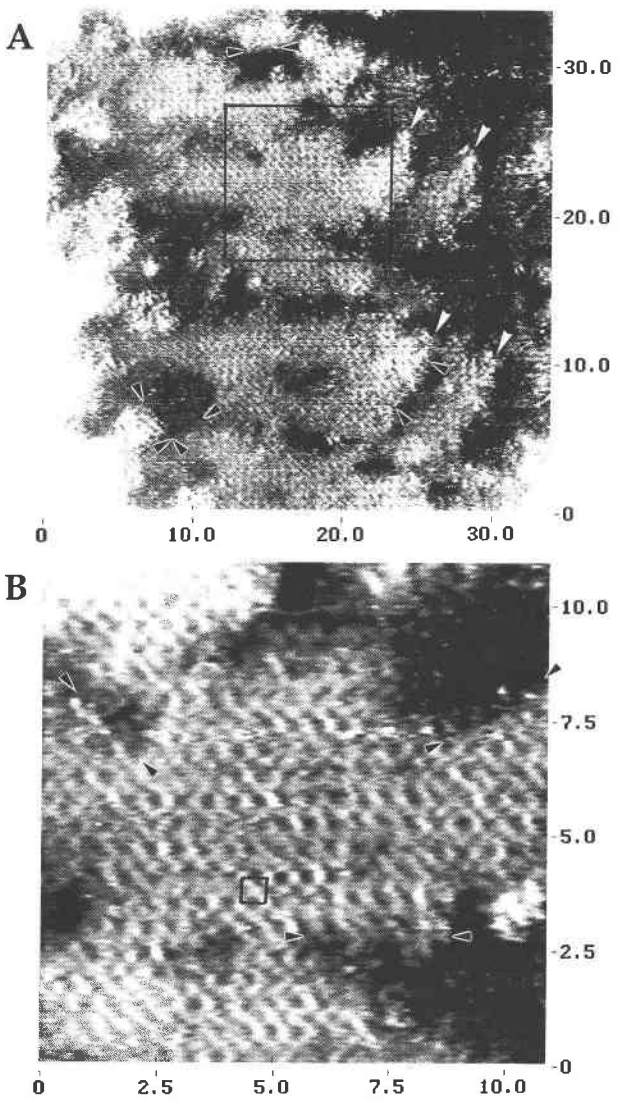

FIGURE 16. In both images, solid arrows show the end points of a few crystallographically oriented borders between oxidized and unoxidized areas. Scales in nanometers. Conditions (both): 1.0 nA, 100.0 mV. **(A)** 34 × 34 nm image. White arrows show surface features that repeat, indicating a double tip. **(B)** Close-up of area marked with a square in A, taken 3 min later than A. A unit cell is marked.

ly oxidized, consistent with the XPS result. The oxidized surface has relatively large oxidized and unoxidized areas rather than randomly oxidized individual sites. The borders between oxidized and unoxidized areas do not follow one crystallographic direction for long distances, but they often occur in short segments in ⟨110⟩ directions, with a smaller number in ⟨100⟩ directions (see solid arrows in Fig. 16A).

Figure 16B shows the area marked in Figure 16A, 3 min later. The pattern of unoxidized areas is almost identical to the earlier image, confirming that little alteration took place during STM imaging for a few minutes. Figure 16B, though still affected by acoustic noise and double-tip artifacts, shows the expected Fe^{2+} substructure (unit cell marked). Solid arrows point to patch borders oriented in ⟨110⟩ or ⟨100⟩ directions.

Figure 17 shows two tiled images of another terrace on the same surface as in Figure 16. Again, borders between light and dark areas occur in short segments in the ⟨110⟩ and ⟨100⟩ directions (solid arrows). As in Figure 16A, the area on the right edge of the imaged areas is completely oxidized, and fingers of oxidation extend leftward

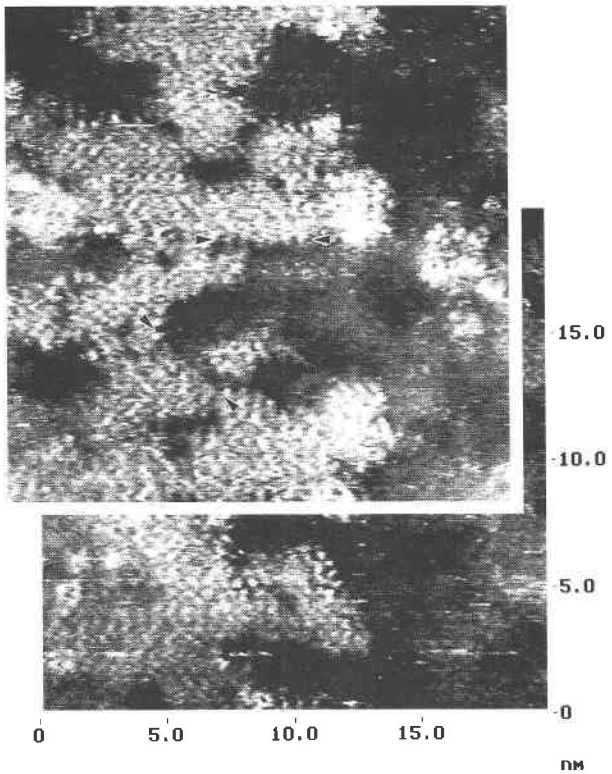

FIGURE 17. Two 20 × 20 nm images tiled together. Conditions: setpoint current = 1.0 nA, bias = 100.0 mV. Solid arrows show the end points of a few examples of crystallographically oriented borders between oxidized and unoxidized areas.

into the terrace, suggesting overall oxidation progress from right to left. The unoxidized portions of the terrace exhibit a few single and double dark (presumably oxidized) sites. In neither Figure 16 nor 17 are the ⟨110⟩ linear defects evident.

We imaged several as-received pyrite surfaces (Fig. 18), i.e., the natural growth surface exposed to air for an unknown number of years. Because these surfaces were "dirty," image noise was severe. We assume that oxidation over many years leads to electronic "topography" that reflects oxidation rather than growth mechanisms. This assumption is probably a good one at the 30–40 nm scale but may not be safe for much larger (≥1 mm) areas and their topography. In Figure 18, the sample was oriented with [100] and [010] parallel to the edges of the image. Borders between light and dark areas are often parallel to ⟨110⟩ directions (a few are marked with arrows). In Figure 18A, two lines are drawn parallel to borders that, though not always parallel to ⟨110⟩ at the microscale, bear an overall trend in this direction. The width of this dark region is similar to the separation of ⟨110⟩ lineations in Figure 12A, suggesting that oxidation reactivity differs from area to area in a way related to defects (see also Martello et al. 1994).

Electron tunneling spectroscopy (ETS) has been used to study the electronic structure of individual surface sites

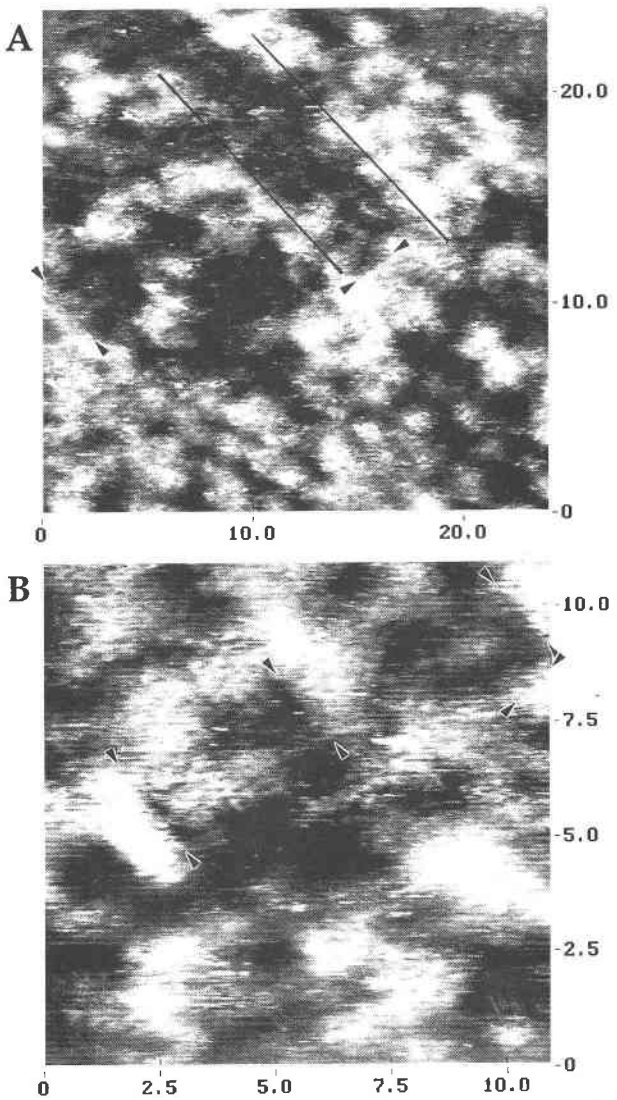

FIGURE 18. STM images of pyrite growth surfaces. Scales in nanometers. (A) Conditions: setpoint current = 1.2 nA, bias = 100.0 mV. Vertical relief is 6 Å. Arrows and lines indicate short segments and overall trends, respectively, of borders between light and dark areas that are parallel to ⟨110⟩. (B) Conditions: 1.2 nA, −100.0 mV. Vertical relief is 3 Å. Arrows indicate segments of oriented reaction borders.

(e.g., Avouris 1990; Crommie et al. 1993) and to distinguish between oxidized and unoxidized regions of galena surfaces (Eggleston and Hochella 1991, 1993, 1994). During continuous spectrum acquisition, with the tip drifting over the surface of the sample shown in Figure 18, two distinctly different types of spectrum were obtained (Fig. 19), one with a higher apparent density of states (DOS) at the top of the VB (type A) than the other (type B). Possibly, the tip encountered relatively fresh surface for spectra of type A and more oxidized surface for spectra of type B. The DOS between −100 and −300 mV (Fig. 19A) would stem from surface states of Fe^{2+}. Using ETS,

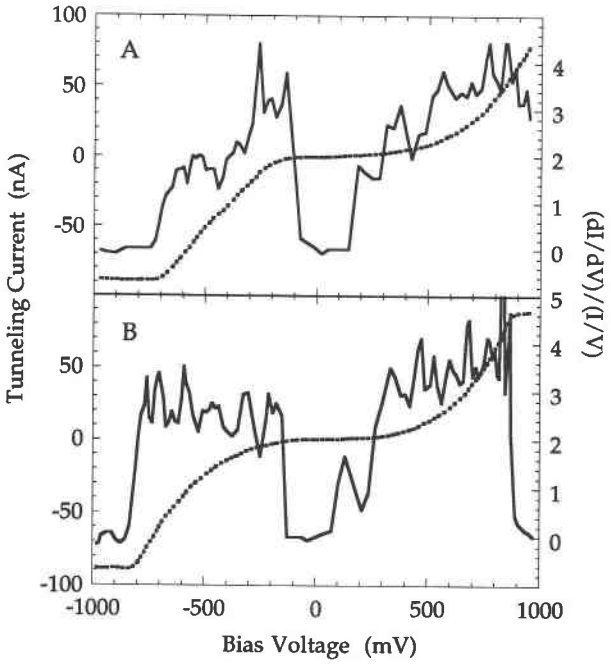

FIGURE 19. ETS of the surface imaged in Figure 18A. Dotted lines refer to the scale on the left, and solid lines refer to the scale on the right. (**A**) Type "A" spectra. (**B**) Type "B" spectra. The raw tunneling current (I) vs. voltage (V) data (dotted lines) are plotted with the function $(dI/dV)/(I/V)$, which approximates the density of states at a given energy level (solid lines).

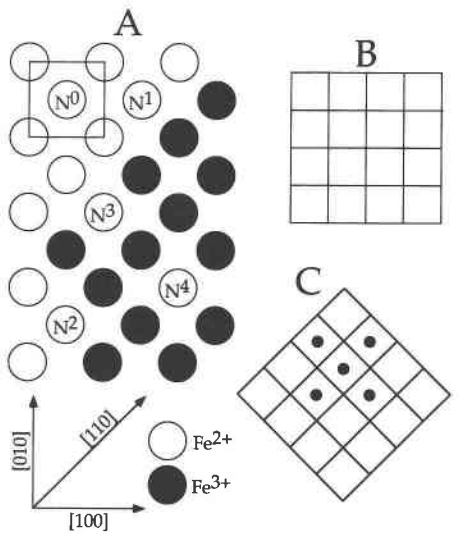

FIGURE 20. (**A**) Definition of surface sites, as described in the text. N^i indexes unoxidized sites by the number i of oxidized nearest neighbors. Unoxidized sites in the next layer down are neglected (see text). (**B**) A square grid, a 100 × 100 example of which was used in the Monte Carlo simulation. (**C**) The square grid axes are related to the unit-cell axes of the pyrite surface by a 45° rotation.

Fan and Bard (1991) showed a fresh-surface band gap comparable to the bulk band gap of pyrite (0.9 eV) and an apparent defect state within the gap. In Figure 19B, the gap appears to be only 0.2 eV, suggesting that the band gap is indeed filled in by surface states. This is consistent with photoelectrochemical studies (e.g., Jaegermann and Tributsch 1988; Fan and Bard 1991; Mishra and Osseo-Asare 1992).

DISCUSSION

Site specificity and autocatalysis

Because Fe^{3+} is an oxidant for pyrite as well as a reaction product, it is natural to inquire if pyrite oxidation is, at least initially, autocatalytic. The idea is that the greater the number of oxidized neighbors (acceptors) around an unoxidized surface site, the greater the probability is that the unoxidized site will oxidize in a given time interval. This notion can be tested using a simple Monte Carlo (MC) simulation.

We first define an N^i site as an Fe^{2+} site with i Fe^{3+} nearest neighbors (Fig. 20). We have a reaction of the form

$$N^i + \text{oxidant} \rightarrow \text{oxidized surface site} + \text{reductant} \quad (7)$$

for which a rate law, first order in each reactant, is

$$\text{rate}_{N^i} = k_{ox}[N^i][\text{oxidant}] \quad (8)$$

where k_{ox} is a rate constant for electron transfer to the oxidant and brackets indicate concentration. If the oxidant is nearest-neighbor Fe^{3+}, then Equation 8 is simply

$$\text{rate}_{N^i} = k_{ox}[N^i](i). \quad (9)$$

Site specificity of rate is contained in i; obviously, this only applies to N^i sites with $i > 0$. For MC calculations, the rate constant is replaced by a probability, i.e.,

$$\text{rate}_{MC,N^i} = P_{ox}[N^i](i) = \{P_{ox}(i)\}[N^i]. \quad (10)$$

Given P_{N^1}, $P_{N^2} = 2P_{N^1}$, $P_{N^3} = 3P_{N^1}$, and so forth; i.e., the rate of oxidation of particular sites becomes proportional to the number of oxidized nearest neighbors.

The MC simulations used a 100 × 100 square-site array (Figs. 20B and 20C show the relation between a square array and the pyrite unit cell). In some experiments, one-half of the area was "pre-oxidized" to create a situation similar to a [100] step on the pyrite surface. A site-accounting routine tracked the number of N^i sites during oxidation progress. Oxidation probabilities for given N^i sites (e.g., P_{N^0}, P_{N^1}, etc.) were input parameters.

Patterns from the various MC experiments (Fig. 21), each for different input parameters, may be compared to Figures 16A and 17. Figures 21A and 21B are the closest match. P_{N^1} through P_{N^4} are proportional to i (Eq. 10) in both cases, which differ only in P_{N^0}. Higher P_{N^0} increases the number of oxidation nuclei on the fresh surface in Figure 21B relative to Figure 21A and increases the number of more reactive (P_{N^i}, $i > 0$) sites initially produced, so that the overall rate is greater (Fig. 21B took 65% of the iterations needed for Fig. 21A). In both cases, several

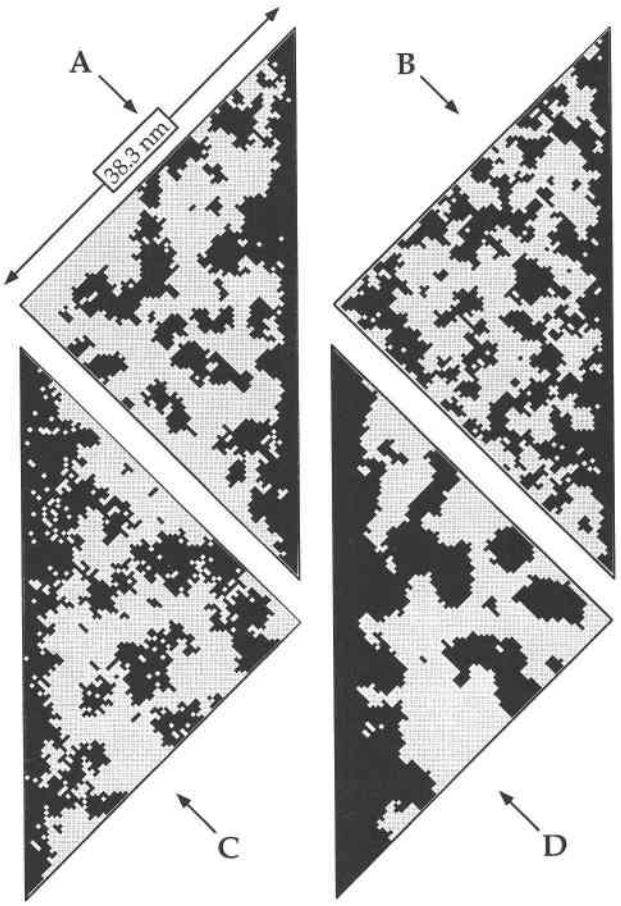

FIGURE 21. Oxidation patterns from the Monte Carlo simulations after an amount of oxidation comparable to that in the STM images in Figures 16A and 17. Reaction probabilities used are, in the order of P_{N^0}, P_{N^1}, P_{N^2}, P_{N^3}, P_{N^4}: **(A)** 0.0004, 0.1, 0.2, 0.3, 0.4; **(B)** 0.002, 0.1, 0.2, 0.3, 0.4; **(C)** 0.0004, 0.1, 0.1, 0.1, 0.1; **(D)** 0.0004, 0.1, 0.4, 0.8, 0.9.

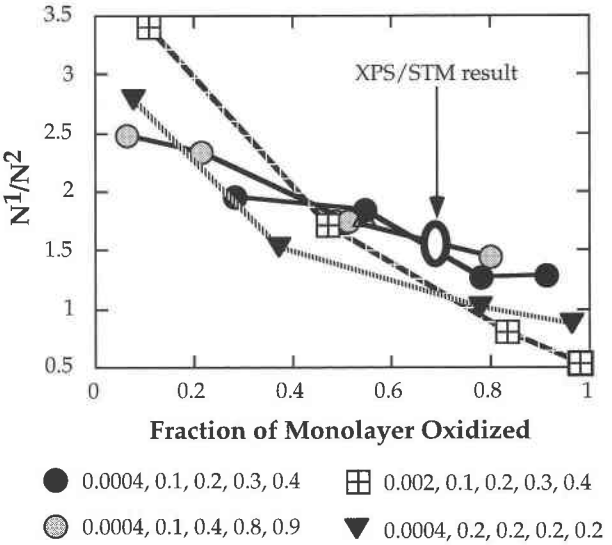

FIGURE 22. Plot of the ratio of the number of N^1 to the number of N^2 sites as a function of the fraction of surface sites oxidized, from the Monte Carlo results, and compared to a value estimated from the STM-XPS results.

edge segments in ⟨110⟩ directions are evident. Figure 21C resulted from making all $P_{N^i} > P_{N^0}$ identical; there are few border segments of any length and too many N^4 sites relative to the STM images. Figure 21D shows the effect of making P_{N^i} for $P_{N^i} > P_{N^0}$ a nonlinear function of i (see caption), which does not match the STM results very well because oxidized patch nuclei grow quickly to a size larger than observed in STM for a similar amount of total oxidation. Because our STM results show only the oxidation of Fe^{2+}, the MC simulations consider only Fe^{2+} sites (S_2 oxidation is ignored). S_2 oxidation is, however, part of a complete chemical model.

Comparison of Monte Carlo results with XPS and STM results

In a square lattice, any model in which reaction probability depends on nearest-neighbor interaction leads to a patchy surface, with patch edges parallel to the axes of the lattice (e.g., see Blum and Lasaga 1987; Wehrli 1989; Lasaga 1990). The STM and MC results for pyrite (001) are thus not surprising because interaction between nearest-neighbor Fe sites occurs in ⟨110⟩ directions (see Fig. 20C). A quantitative comparison between the STM and MC results can be made by plotting the ratio of the number of N^1 sites to the number of N^2 sites (abbreviated N^1/N^2) against the fraction of surface sites oxidized. This ratio is a measure of the relative enrichment of the surface in sites along ⟨110⟩-oriented borders (N^1) vs. those along ⟨100⟩-oriented borders (N^2, see Fig. 20A). We used the XPS Fe 2p data to quantify the fraction of oxidized sites; the N^1/N^2 ratio was determined by counting individual sites in the STM images. The XPS results have an uncertainty of ±10%. The STM results are based on counting of sites in the clearest images, but some subjectivity is inevitable in classifying sites. Results are plotted in Figure 22, along with MC results for various starting conditions. In two cases, the results are significantly different from the XPS and STM results and from the other MC results; these correspond to all $P_{N^i} > P_{N^0}$ being identical and to a large P_{N^0}/P_{N^1} ratio.

Because of the uncertainties inherent in XPS and STM, and because the MC surface pattern is not extremely sensitive to the relative reaction probabilities, our conclusions are approximate. With this caveat, however, we conclude that a P_{N^0}/P_{N^1} ratio of between 10^{-3} and 10^{-2}, and P_{N^i} (for $P_{N^i} > P_{N^0}$) proportional to i, approximates the STM and XPS results well. This conclusion is consistent with autocatalytic initial oxidation.

Electronic structure and surface states

During initial pyrite oxidation, patches of a ferric oxide or oxyhydroxide product form. These small and extremely thin patches constitute surface states. We model these

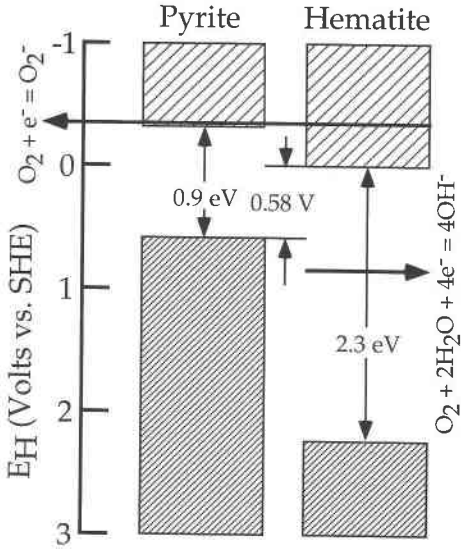

FIGURE 23. Band edges of pyrite (Wei and Osseo-Asare 1995) and hematite (Hoffmann 1990), and the O_2 reduction potential (Sawyer 1991), vs. SHE at pH = 7.

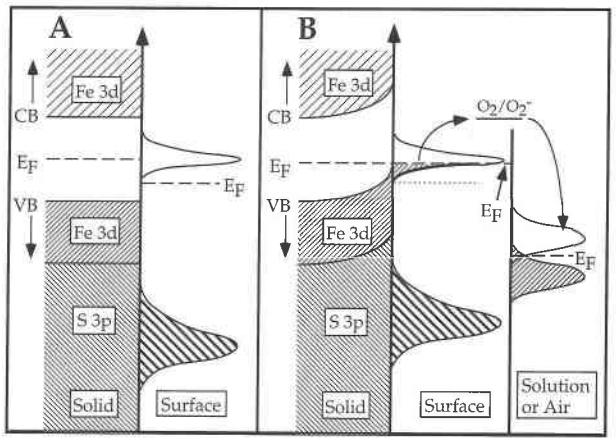

FIGURE 24. (**A**) Band structure of the bulk and surface of pyrite, given the formation of an oxide (hematite-like) surface state. The unfilled and bold-cross-hatched "peaks" represent the CB and VB of a hematite-like surface state, respectively. (**B**) Band bending resulting from equilibration between the pyrite bulk and surface, including the hematite-like surface states (see text). Electron transfer to O_2 is shown, along with subsequent breakdown of O_2^- to form H_2O eventually. The Fermi level, E_F, is specific to each phase.

surface states using the band edges of hematite, although hematite is less likely to resemble the initial product than are $Fe(OH)_3$, FeOOH, and ferric hydroxysulfates (because patches are initially very thin and of limited areal extent, they cannot be considered bulk phases). For discussion purposes we assume hematite band edges can be used because its band-edge positions are relatively well known and probably do not vary drastically from different ferric oxyhydroxides (e.g., Leland and Bard 1987).

Figure 23 shows the band edges of pyrite and hematite at pH = 7, vs. the standard hydrogen electrode (SHE). All potentials shift downward (i.e., toward positive Eh in Fig. 23) with decreasing pH, but their relative positions do not shift.

The STM and MC results suggest that product Fe^{3+} can accept electrons from pyrite Fe^{2+}. This is equivalent to electron transfer (ET) from the pyrite VB to the CB of the oxide product. The O_2-O_2^- couple ($E^\circ = -0.33$ V at 0.2 atm O_2, pH = 7; Sawyer 1991) lies above both the VB of pyrite and the CB minimum of hematite, so that ET to O_2 is energetically uphill (activated) in both cases. This electrochemical scheme is shown in Figure 24A. At the surface, the Fe^{2+} site symmetry is broken, resulting in subsplitting of the Fe 3d t_{2g} and e_g crystal-field states (see Jaegermann and Tributsch 1988), but such surface states are omitted for clarity. Upon formation of small amounts of ferric oxide, the surface states in Figure 24 appear. The pyrite Fermi level is placed at mid gap, and the hematite Fermi level is placed at the top of its band gap in anticipation of n-type conduction in the oxide.

If the pyrite is n-type pyrite (i.e., it has a small population of CB electrons), formation of the oxidation product creates an empty band (oxide CB) into which these electrons can be transferred, creating a depletion layer in the pyrite surface region (Fig. 24B). This is related to Fermi-level pinning by surface states (examined for pyrite by Mishra and Osseo-Asare 1992) and results from equilibration of bulk and surface Fermi levels. The Fermi level represents a chemical potential; at equilibrium, the chemical potential is everywhere the same, so the Fermi level must be flat across the interface at equilibrium. Removal of electrons from the surface region thus corresponds to upward bending of the bands.

We consider ET from surface states to O_2 as the rate-limiting step (Fig. 24B). Later breakdown of O_2^- by consumption of H^+ to form H_2O (illustrated in Fig. 24B as a donor-acceptor pair in solution) leads to the formation of the highly oxidizing, transient intermediates $OH^\cdot$ and H_2O_2. The familiar four-electron reaction, $O_2 + 4H^+ + 4e^- = 2H_2O$ ($E^\circ = 1.23 - 0.059\text{pH} + 0.0148 \log P_{O_2}$ V), is a combination of four elementary steps involving these intermediates (e.g., see Stumm and Morgan 1996).

Electron-transfer rates

We are now prepared to estimate rate constants for elementary ET steps in pyrite oxidation that are consistent with the STM, XPS, and MC results. Our questions are as follows: (1) Can we safely ignore ET to second-nearest-neighbor Fe^{3+}, as the Monte Carlo model has assumed? (2) What are the relative rates of ET to O_2 from the pyrite VB and from the hematite CB? (3) Is it appropriate to model electron exchange between the pyrite VB and hematite CB as an equilibrium? (4) What ET steps are rate controlling?

We can assess relative and absolute ET rate constants using Marcus theory (Appendix). The rate constant for electron transfer k_{ET} is written

$$k_{ET} = \nu_n \kappa_{el} \kappa_n \qquad (11)$$

where ν_n is an attempt frequency, and κ_{el} and κ_n are transfer coefficients for interaction of degenerate donor and acceptor electronic states and for changes in atomic positions needed to bring electronic states into degeneracy, respectively.

Question 1. For site-to-site ET as a function of distance between sites, ν_n and κ_n do not change, and we need only consider κ_{el} (e.g., Graetzel 1989):

$$\kappa_{el} = \kappa_{el,0} \exp[-\beta(r - r_0)] \quad (12)$$

where r is the distance of interest, and $\kappa_{el,0}$ is κ_{el} at reference distance r_0. For isolated atomic Fe 3d orbitals, $\beta = 1.64 \times 10^{11}$ m^{-1}. The difference in distance $(r - r_0)$ for nearest- and second-nearest-neighbor Fe at the pyrite surface is 1.59 Å, giving $\kappa_{el}/\kappa_{el,0} = 4.7 \times 10^{-12}$; ET to second-nearest neighbors is thus negligible. However, β in crystals may be smaller than for isolated atoms. Decreasing β by an order of magnitude (an exaggeration), we have $\kappa_{el}/\kappa_{el,0} = 7.4 \times 10^{-2}$, so ET to second-nearest-neighbor Fe^{3+} remains relatively unimportant.

Question 2. For N^0 sites oxidizing in air (or, more precisely, in the thin water film formed on solid surfaces in contact with humid air), we invoke the following reaction between surface sites and O_2 molecules:

$$Fe^{2+}_{N^0,S} + O_2 \rightarrow Fe^{3+}_{S} + O_2^- \quad (k_1). \quad (13)$$

The S subscript identifies sulfur as the primary coordinating anion. Here and below, the k_j is the jth rate constant. For N^i $(i > 0)$ sites, we postulate a two-step alternative pathway (pathway 1 in Fig. 25):

$$Fe^{2+}_{edge,S} + Fe^{3+}_{edge,O} = Fe^{3+}_{edge,S} + Fe^{2+}_{edge,O} \quad (k_2, k_{-2}) \quad (14)$$

$$Fe^{2+}_{edge,O} + O_2 \rightarrow Fe^{3+}_{edge,O} + O_2^- \quad (k_4) \quad (15)$$

in which the subscript "edge" identifies Fe at an edge between oxidized and unoxidized areas, and the S or O subscript identifies the primary (though not necessarily exclusive) coordinating anion. The hypothesized Fe coordination environments are consistent with possible contributors to the tail-off in the Fe 2p ½ XPS spectra. Equation 14 describes ET from the pyrite VB to the oxide CB, and Equation 15 describes ET from the oxide CB to O_2. Below, we consider the relative rates for the reactions in Equations 13 and 15.

Rate constants for heterogeneous ET can be estimated from the following expression, which is based on Marcus theory (e.g., see Sutin 1983) and Equation 11:

$$k_{ET,het} = \nu_n \kappa_{el} \exp\left[\frac{-(\lambda + \Delta G^{o\prime})^2}{4kT\lambda}\right] \quad (16)$$

in which $\Delta G^{o\prime}$ is the overall thermodynamic driving force ($\Delta G^{o\prime} = E_{sfc} - E^{o\prime}$, where E_{sfc} is the energy level of the donor state at the surface, and $E^{o\prime}$ is the reduction potential of the acceptor molecule). The reorganization energy λ is defined in the Appendix. For ET to O_2 from an oxide surface, λ is taken to be ~1 eV (λ for the solid surface is small relative to that of O_2; Goodenough 1972; Kesselmann et al. 1994).

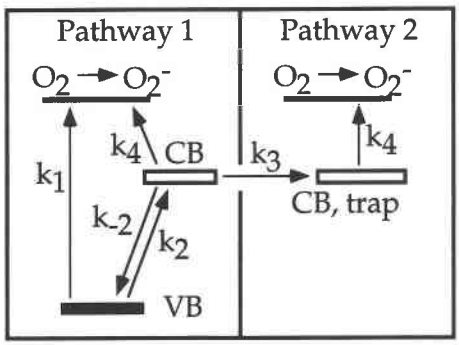

FIGURE 25. Illustration of the alternative reaction pathways discussed in the text. The vertical axis corresponds to the energy level. Pathway 1 includes both direct VB-to-O_2 ET (k_1) and an equally fast pathway described by equilibrium with the CB of the oxide product. In pathway 2, electrons that reach the oxide CB are trapped (k_3) before they transfer to O_2 (k_4). Rate constants for each process correspond to those in the text.

We are comparing ET from Fe^{2+} to O_2 in both cases, so $\Delta G^{o\prime}$ is probably the only variable to change significantly. The $\Delta G^{o\prime}$ value for ET from the VB of pyrite to O_2 is estimated to be 0.88 eV, and for ET from the CB of hematite to O_2 it is estimated to be 0.33 eV. Therefore,

$$\frac{k_{ET,pyr,VB}}{k_{ET,hem,CB}} = \exp\left[\frac{-(\lambda + \Delta G^{o\prime}_{pyr,VB})^2}{4kT\lambda}\right] \Big/ \exp\left[\frac{-(\lambda + \Delta G^{o\prime}_{hem,CB})^2}{4kT\lambda}\right] = 3.4 \times 10^{-8}. \quad (17)$$

This ratio is approximate because the band-edge positions that determine $\Delta G^{o\prime}$ (Fig. 23) are not precisely known, but it is probably accurate within an order of magnitude.

A related way to estimate the rates of Equations 13 and 15 is found in a linear free-energy relation (LFER) by Wehrli (1990) for oxidation of Fe^{2+}_{aq} and other metal cations by O_2. This LFER has been used to estimate oxidation rates of Fe^{2+} on surfaces (Wehrli 1990; Stumm and Sulzberger 1992). The LFER is simply

$$\log k_i = \log k_0 + \Delta E_i^\circ/0.059 \quad (18)$$

so that $\Delta \log k = [\Delta E_1^\circ - \Delta E_2^\circ]/0.059$. For $\Delta E_1^\circ - \Delta E_2^\circ$, we use the difference between the pyrite VB and the hematite CB (0.58 eV), giving $\Delta \log k = 9.83$. Overall, these approaches both suggest that oxidation by O_2 of the pyrite VB should be roughly nine orders of magnitude slower than that of CB electrons from hematite.

Question 3. Equation 14 describes intrasurface ET, similar to n-type conduction by electron hopping. For hematite, the activation energy for site hopping by electrons at 25 °C is <0.1 eV (Goodenough 1972). The activation energy of n-type conduction is smaller in pyrite than in hematite (Shuey 1975). Therefore, for ET between neighboring surface sites, hematite-like λ domi-

TABLE 4. Approximate rate constants for electron transfer between various species involved in pyrite oxidation (from Marcus cross relation, Eq. A-2)

ET process	k_{11} (s^{-1})	k_{22} (s^{-1})	log K_{12}	log f	k_{ET} (s^{-1})
VB(1) to O_2(2)	1.08×10^{11}	1.18×10^{8}	−14.88	−10.1	1.2×10^{-3}
CB(1) to O_2(2)	1.08×10^{11}	1.18×10^{8}	−5.58	−1.42	1.13×10^{6}
VB(1) to CB(2)	1.08×10^{11}	1.08×10^{11}	−9.81	−9.49	24.2
CB(1) to VB(2)	1.08×10^{11}	1.08×10^{11}	9.81	−9.49	1.6×10^{11}

nates. By Marcus theory, $\lambda = 4\Delta G^* < 0.4$ eV; we assume 0.3 eV. Goodenough (1972) concluded that $\nu_0 = 2 \times 10^{12}$ s^{-1} (which includes the effect of κ_{el}) is a good approximation for hematite. We used this value in all of our calculations. Self-exchange rate constants were calculated from Equation A-1 in the Appendix and listed in Table 4. Table 4 does not account for collision frequency or electrostatic effects for surface-to-O_2 ET. These approximations are intended to compare only roughly the resulting rate constants with those for ET to O_2. The most important results are (1) the rate for the CB-to-VB transition is far faster than that for ET to O_2, so that treating Equation 14 as an equilibrium appears reasonable; and (2) similar to the calculation under Question 2 above, the rate for ET to O_2 is about nine orders of magnitude faster from the oxide CB than from the pyrite VB.

Treating the VB-to-CB reaction as an equilibrium leaves us with, for Equation 13, rate = k_1[e⁻,VB]; and for Equations 14 and 15, rate = k_4K[e⁻,VB], where $K = k_2/k_{-2}$ (Eq. 14). The degree to which k_4 is larger than k_1 (Eq. 17 or LFER result) is canceled by K (Table 4). Both pathways (Eq. 13 vs. Eqs. 14 and 15) would thus be about equally fast. Therefore, equilibrium between the pyrite VB and the oxide CB cannot describe the experimental and MC results.

To bring theory in line with observation, we must add a reaction that decreases the rate of back reaction in Equation 14. One possibility is that the product species $Fe^{3+}_{edge,S}$ is a precursor to S_2 oxidation by Fe^{3+} to reform Fe^{2+} and thus disallow back reaction. Another possibility is that electrons in the $Fe^{2+}_{edge,O}$ sites hop to Fe^{3+} sites deeper in the oxide patch before they hop back to the original site (similar to k_{11} for oxide self-exchange in Table 4), in effect "trapping" the electron in the oxide CB. Both possibilities are combined in Equation 19, with rate constant k_3:

$$Fe^{2+}_{edge,O} + \text{trap} \rightarrow Fe^{2+}_{O,trap} \qquad (k_3). \tag{19}$$

We simply postulate a reaction that traps electrons in the oxide CB. S_2 oxidation and electron hopping clearly occur in the pyrite oxidation process and thus constitute reasonable reactions to which we can appeal.

Considering kinetic equations and applying the steady-state approximation for intermediate species, we find that the effective (pseudo first-order) rate constant for O_2 reduction is $k_1[Fe^{2+}_S]$ in Equation 13 (pathway 1) and

$$\{k_2k_3[Fe^{3+}_{edge,O}][\text{trap}]/(k_{-2}[Fe^{3+}_{edge,S}] + k_3[\text{trap}])\}[Fe^{2+}_{edge,S}] \tag{20}$$

in Equations 14, 15, and 19 (pathway 2). This can be greatly simplified by realizing that all the species in Equation 20, except possibly [trap], are surface species. For example, $[Fe^{3+}_{edge,O}]$ is simply i in Equation 9. By the same token, $[Fe^{3+}_{edge,S}] = 1$, because in any VB-to-CB hopping event, only one $Fe^{3+}_{edge,S}$ site is created and available for back reaction. Thus, Equation 20 can be simplified to

$$(i)k_2\text{M}[Fe^{2+}_{edge,S}] \tag{21}$$

where $\text{M} = k_3[\text{trap}]/(k_{-2} + k_3[\text{trap}])$. The substitutions made to obtain Equation 21 follow an equation in Goodenough (1972) describing n-type conduction in hematite by activated electron hopping from metal center to metal center:

$$\tau_{hop}^{-1} = n^+\tau_0^{-1} \exp[-\Delta G_{def}/kT] \tag{22}$$

where τ_{hop} is the time between hopping events, τ_0 is a time between attempts, $\Delta G_{def} = \lambda/4$ (Appendix), and n^+ is the number of possible destinations for the hop ($n^+ = i$ in Eq. 9). Equation 22 resembles Equation A-1 ($k_{se} = \nu_{0,se}\exp[\lambda_{se}/4kT]$) if $\nu_0 = \tau_0^{-1}$. With these substitutions, and including $\Delta G^{o\prime}$ to account for differing donor and acceptor energy levels (Eq. 16), we have

$$k_{i,\text{VB}\rightarrow\text{CB}} = (i)\nu_n\kappa_{el}\exp\left[\frac{-(\lambda + \Delta G^{o\prime})}{4kT\lambda}\right] \tag{23}$$

or

$$k_{i,\text{VB}\rightarrow\text{CB}} = (i)k_{\text{VB}\rightarrow\text{CB}} = (i)k_2. \tag{24}$$

The rate constant for oxidation of N^i sites is simply the product of a rate constant for ET between individual donor and acceptor sites (e.g., k_{ET} for the VB-to-CB transition, Table 4) and the number of destinations (acceptor sites) with which the donor can react, i. The rate constant $k_{\text{VB}\rightarrow\text{CB}}$ can be equated with k_2 in Equation 14. Equation 24 resembles the rate constant in Equation 9, used in the MC simulation of the STM and XPS results.

What value of k_3 is needed to ensure that pathway 2 (Fig. 25) is two to three orders of magnitude faster than pathway 1, as suggested by the MC results? Using estimates of k_2 (VB to CB) and k_{-2} (CB to VB) from Table 4, we find

$$k_1/\{k_2k_3[\text{trap}]/(k_{-2} + k_3[\text{trap}])\} = 3 \times 10^{-3}$$

$$k_3[\text{trap}] = 1.84 \times 10^{10}. \tag{25}$$

The trapping reaction(s) must be fast but not unreasonably fast. For example, electron hopping to sites deeper

in the oxide patch, equivalent to self-exchange within the oxide, is described by a rate constant of 10^{11} s^{-1} (k_{11}, Table 4). The value of [trap] in this case would again be an integer directly analogous to n^+ in Equation 22.

Question 4. By assuming a fast trapping reaction we avoid the VB-CB equilibrium problem so that ET from the pyrite VB at the surface to neighboring Fe^{3+} sites (oxide CB) is rate controlling. The proportionality between the oxidation probability of N^i sites and i (Eq. 9) is preserved in Equations 23 and 24. Oxidants other than O_2, such as Fe^{3+}_{aq} or a bacterial biomolecule, can be understood within the same framework if $\Delta G^{o\prime}$ and λ can be quantified (Eq. 16).

Because S 3p states lie deeper in the pyrite VB than Fe 3d states, ET to O_2 from S_2 is much slower than from Fe^{2+}. S_2 oxidation may play a role in the trapping reaction by donating electrons to nearest-neighbor Fe^{3+} as discussed above, but it might also be coupled to Fe^{2+} oxidation by reacting with strong transient oxidizing agents that result from O_2 reduction, such as peroxy radicals (HO_2), hydrogen peroxide (H_2O_2), and hydroxyl radicals ($OH^{\cdot}$). Pyrite oxidation is pseudo first order in H_2O_2 concentration (McKibben and Barnes 1986), for example. Some decoupling of Fe^{2+} and S_2 oxidation rates allows for the differing amounts of oxide vs. sulfate and sulfate vs. polysulfide, oxidation products observed under different conditions (e.g., see Lowson 1982).

A generalized (but not stoichiometrically balanced in detail) reaction sequence consistent with our observations is given in Figure 26 (possible dissolution steps are not included). This model is generally consistent with other models for pyrite oxidation. The sluggishness of Fe^{2+} oxidation by O_2 and Fe^{3+}-Fe^{2+} redox cycling are prominent in the Singer and Stumm (1970) and Moses and Herman (1991) models. Branching of the sulfate pathway away from the polysulfide pathway, such that polysulfide is not an intermediate in sulfate formation, is consistent with the study of Biegler and Swift (1979). By assuming that all heterogeneous oxidation reactions are outer-sphere, our model is consistent with the work of Taylor et al. (1984a, 1984b) and Reedy et al. (1991), in which O in SO_4^{2-} is derived mostly from H_2O rather than from O_2 (oxidation of pyrite in air involves H_2O, which adsorbs to the surface from air).

We considered only intrasurface electron transfer at reaction borders moving laterally across the surface and did not considered the reaction border parallel to the surface that underlies the oxidized patches. This is because, for the second layer, although electron exchange can be just as rapid as elsewhere, the O or other molecular species that may be needed for the trapping reaction cannot as easily reach the $Fe^{3+}_{edge,S}$ sites. The overall oxidation reaction, even after only a monolayer of oxidation, becomes rate limited by atom transport through the product layer rather than by electron transport. Figure 19 shows, however, that the importance of particular crystallographic directions, and thus of particular surface sites, appears to be similar in both long-term and initial oxidation.

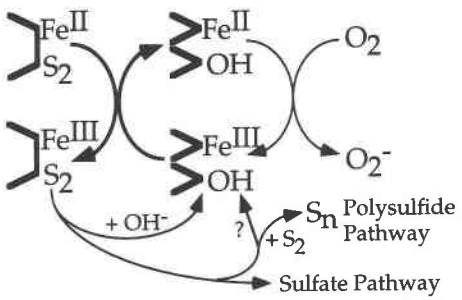

FIGURE 26. Illustration of the oxidation mechanism. In upper left, electron exchange between fresh pyrite and oxide-like sites takes place. The oxide-like Fe species act as intermediates between pyrite and O_2. Outer-sphere oxidation of S_2, or electron hopping in the oxide, traps electrons in the oxide conduction band. A ligand-exchange step is included to symbolize creation of oxide-like Fe^{3+} sites from $Fe^{3+}_{edge,S}$ sites.

IMPLICATIONS

We used XPS, UPS, and STM to constrain a model of electron-transfer kinetics during initial oxidation of pyrite surfaces. XPS and UPS showed the loss of fresh surface states (e.g., Fe^{2+}) and gain of product states (e.g., Fe^{3+}) during oxidation in air. STM showed the surface distribution of Fe^{2+} states; oxidized areas occur in patches having shapes that were reproduced using a Monte Carlo model in which the probability of Fe^{2+} oxidation is proportional to the number of oxidized (Fe^{3+}) nearest neighbors. Surface Fe^{3+}-Fe^{2+} redox cycling is clearly important in pyrite oxidation (e.g., Moses and Herman 1991); here, we showed in some detail how such cycling occurs at edges between oxidized and unoxidized areas and described the kinetics using Marcus theory. We used $\Delta G^{o\prime}$ values from the band edges of surface states, and reorganization energies from the activation energy of conduction in iron oxide semiconductors. Although this approach is new within geochemistry, similar models have been used to describe electron transfer at oxide surfaces in the photoelectrochemical field (e.g., see Graetzel 1989; Kesselmann et al. 1994).

Although our specific goal has been a new description of interfacial electron transfer during pyrite oxidation, the approach has general applicability in geochemical studies of redox processes involving solid surfaces. First, redox potentials of species at mineral surfaces can be understood from the band structures of the bulk solid and of surface states. Second, the redox potential of a given chemical species (e.g., Fe^{2+}) may vary considerably depending on its specific surface-coordination environment, much as hydrolysis in aqueous solution changes redox potentials of metal ions. Third, Marcus theory can be applied to the kinetics of electron transfer across mineral-water and mineral-air interfaces by using the electronic structure (band structure and conductivity characteristics) of the solid and its surface states (or of carefully chosen analogs).

XPS-UPS and STM results provide complementary in-

formation and help to constrain proposed oxidation mechanisms in a way not previously possible. STM helps to extend the usefulness of previously available spectroscopic techniques and better defines the surfaces and surface sites that act as key reactants in natural systems.

Acknowledgments

This research was made possible by funding from the Swiss National Science Foundation and the CNRS, France. C.M.E. thanks Barbara Sulzberger, Stephan Hug, and Kevin Knauss for their support and dedicates this work to Noye M. Johnson. The manuscript benefited greatly from thorough and thoughtful reviews by C.O. Moses, K. Rosso, and two anonymous reviewers.

References cited

Avouris, P. (1990) Atom-resolved surface chemistry using the scanning tunneling microscope. Journal of Physical Chemistry, 94, 2246–2256.

Bakken, B.M., Hochella, M.F., Jr., Marshall, A.F., and Turner, A.M. (1989) High resolution microscopy of gold in unoxidized ore from the Carlin mine, Nevada. Economic Geology, 84, 171–179.

Barton, P. (1978) The acid mine drainage. In J.O. Nriagu, Ed., Sulfur in the environment: Part II. Ecological impacts, p. 313–358. Wiley Interscience, New York.

Biegler, T., and Swift, D.A. (1979) Anodic behaviour of pyrite in acid solutions. Electrochimica Acta, 24, 415–420.

Blum, A.E., and Lasaga, A.C. (1987) Monte Carlo simulation of surface reaction rate laws. In W. Stumm, Ed., Aquatic surface chemistry: Chemical processes at the particle-water interface, p. 255–292. Wiley, New York.

Brion, D. (1980) Etude par spectroscopy de photoelectrons de la degradation superficielle de FeS_2, $CuFeS_2$, ZnS, and PbS a l'air dans l'eau. Applied Surface Science, 5, 133–152.

Buckley, A.N., and Woods, R. (1987) The surface oxidation of pyrite. Applied Surface Science, 27, 437–452.

Bullett, D.W. (1982) Electronic structure of 3d pyrite- and marcasite-type sulphides. Journal of Physics C, 15, 6163–6174.

Calmano, W., Förstner, U., and Hong, J. (1994) Mobilization and scavenging of heavy metals following resuspension of anoxic sediments from the Elbe river. In American Chemical Society Symposium Series, 550, 298–321.

Crommie, M.F., Lutz, C.P., and Eigler, D.M. (1993) Spectroscopy of a single adsorbed atom. Physical Review B, 48, 2851–2854.

Eggleston, C.M. (1994) High resolution scanning probe microscopy: Tip-surface interaction, artifacts, and applications in mineralogy and geochemistry. In Clay Minerals Society Workshop Lectures, 7, 1–90.

Eggleston, C.M., and Hochella, M.F., Jr. (1991) Scanning tunneling microscopy of galena surface oxidation and sorption of aqueous gold. Science, 254, 983–986.

——— (1992) Scanning tunneling microscopy of pyrite {100}: Surface structure and step reconstruction. American Mineralogist, 77, 221–224.

——— (1993) Tunneling spectroscopy applied to PbS (001) surfaces: Fresh surfaces, oxidation, and sorption of aqueous Au. American Mineralogist, 78, 877–883.

——— (1994) Atomic and electronic structure of PbS (001) and chemisorption-oxidation reactions. In American Chemical Society Symposium Series, 550, 201–222.

Ennaoui, A., Fiechter, S., Jaegermann, W., and Tributsch, H. (1986) Photoelectrochemistry of highly quantum efficient single-crystalline n-FeS_2 (pyrite). Journal of the Electrochemical Society, 133, 97–106.

Fan, F.-R., and Bard, A.J. (1991) Scanning tunneling microscopy and tunneling spectroscopy of n-type iron pyrite (n-FeS_2) single crystals. Journal of Physical Chemistry, 95, 1969–1976.

Garrels, R.M., MacKenzie, F.T., and Hunt, C. (1973) Chemical cycles and the global environment, 206 p. William Kaufmann, Los Altos, California.

Gerischer, H. (1991) Electron-transfer kinetics of redox reactions at the semiconductor-electrolyte contact: A new approach. Journal of Physical Chemistry, 95, 1356–1359.

Gerischer, H., and Heller, A. (1991) The role of oxygen in photooxidation of organic molecules on semiconductor particles. Journal of Physical Chemistry, 95, 5261–5267.

——— (1992) Photocatalytic oxidation of organic molecules at TiO_2 particles by sunlight in aerated water. Journal of the Electrochemical Society, 139, 113–118.

Goodenough, J.B. (1972) Metallic oxides. Progress in Solid State Chemistry, 5, 145–399.

Graetzel, M. (1989) Heterogeneous photochemical electron transfer, 159 p. CRC Press, Boca Raton, Florida.

Gupta, R.P., and Sen, S.K. (1975) Calculation of multiplet structure of core p-vacancy levels II. Physical Reviews, 12, 15–19.

Harvey, D.T., and Linton, R.W. (1981) Chemical characterization of hydrous ferric oxides by X-ray photoelectron spectroscopy. Analytical Chemistry, 53, 1684–1688.

Hendewerk, M., Salmeron, M., and Somorjai, G.A. (1986) Water adsorption on the (001) plane of Fe_2O_3: An XPS, UPS, Auger, and TPD study. Surface Science, 172, 544–556.

Hochella, M.F., Jr. (1988) Auger electron and X-ray photoelectron spectroscopies. In Mineralogical Society of America Reviews in Mineralogy, 18, 573–637.

Hoffmann, M.R. (1990) Catalysis in aquatic environments. In W. Stumm, Ed., Aquatic chemical kinetics, p. 71–111. Wiley, New York.

Jaegermann, W., and Tributsch, H. (1988) Interfacial properties of semiconducting transition metal chalcogenides. Progress in Surface Science, 19, 1–167.

Jean, G.E., and Bancroft, G.M. (1985) An XPS and SEM study of gold deposition at low temperature on sulphide minerals. Geochimica et Cosmochimica Acta, 49, 979–987.

Jones, C.F., LeCount, S., Smart, R.S., and White, T.J. (1992) Compositional and structural alteration of pyrrhotite surfaces in solution: XPS and XRD studies. Applied Surface Science, 55, 65–85.

Karthe, S., Szargan, R., and Suoninen, E. (1993) Oxidation of pyrite surfaces: A photoelectron spectroscopic study. Applied Surface Science, 72, 157–170.

Kesselmann, J.M., Shreve, G.A., Hoffmann, M.R., and Lewis, N.A. (1994) Flux-matching conditions at TiO_2 photoelectrodes: Is interfacial electron transfer to O_2 rate-limiting in the TiO_2-catalyzed photochemical degradation of organics? Journal of Physical Chemistry, 98, 13385–13395.

Kriegman-King, M.R., and Reinhard, M. (1994) Transformation of carbon tetrachloride by pyrite in aqueous solution. Environmental Science and Technology, 28, 692–700.

Kurtz, R.L., and Henrich, V.E. (1987) Surface electronic structure and chemisorption on corundum transition-metal oxides: α-Fe_2O_3. Physical Review B, 36, 3413–3421.

Lasaga, A.C. (1990) Atomic treatment of mineral-water surface reactions. In Mineralogical Society of America Reviews in Mineralogy, 23, 17–85.

Leland, J.K., and Bard, A.J. (1987) Photochemistry of colloidal semiconducting iron oxide polymorphs. Journal of Physical Chemistry 91, 5076–5083.

Li, E.K., Johnson, K.H., Eastman, D.E., and Freeouf, J.L. (1974) Localized and bandlike valence electron states in FeS_2 and NiS_2. Physical Review Letters, 32, 470–472.

Lowson, R.T. (1982) Aqueous oxidation of pyrite by molecular oxygen. Chemical Reviews, 82, 461–497.

Marcus, R.A. (1965) On the theory of electron-transfer reactions: VI. Unified treatment for homogeneous and electrode reactions. Journal of Chemical Physics, 43, 679–701.

Martello, D.V., Vecchio, K.S., Diehl, J.R., Graham, R.A., Tamilia, J.P., and Pollack, S.S. (1994) Do dislocations and stacking faults increase the oxidation rate of pyrites? Geochimica et Cosmochimica Acta, 58, 4657–4665.

Matheson, L.J., and Tratnyek, P.G. (1994) Reductive dehalogenation of chlorinated methanes by iron metal. Environmental Science and Technology, 28, 2045–2053.

McIntyre, N.S., and Zetaruk, D.G. (1977) X-ray photoelectron spectroscopic studies of iron oxides. Analytical Chemistry, 49, 1521–1529.

McKibben, M.A., and Barnes, H.L. (1986) Oxidation of pyrite in low

temperature acidic solutions: Rate laws and surface textures. Geochimica et Cosmochimica Acta, 50, 1509–1520.

Mills, P., and Sullivan, J.L. (1983) A study of the core level electrons in iron and its three oxides by means of X-ray photoelectron spectroscopy. Journal of Physics D: Applied Physics, 16, 723–732.

Mishra, K.K., and Osseo-Asare, K. (1992) Fermi-level pinning at pyrite (FeS_2)/electrolyte junctions. Journal of the Electrochemical Society, 139, 749–752.

Moore, J.N., and Luoma, S.N. (1990) Hazardous wastes from large-scale metal extraction. Environmental Science and Technology, 24, 1278–1285.

Morse, J.W. (1994) Release of toxic metals via oxidation of authigenic pyrite in resuspended sediments. In American Chemical Society Symposium Series, 550, 289–297.

Moses, C.O., Nordstrom, D.K., Herman, J.S., and Mills, A.L. (1987) Aqueous pyrite oxidation by dissolved oxygen and by ferric iron. Geochimica et Cosmochimica Acta, 51, 1561–1571.

Moses, C.O., and Herman, J.S. (1991) Pyrite oxidation at circumneutral pH. Geochimica et Cosmochimica Acta, 55, 471–482.

Mycroft, J.R., Bancroft, G.M., McIntyre, N.S., Lorimer, J.W., and Hill, I.R. (1990) Detection of sulphur and polysulphides on electrochemically oxidized pyrite surfaces by X-ray photoelectron spectroscopy and Raman spectroscopy. Journal of Electroanalytical Chemistry, 292, 139–152.

Nesbitt, H.W., and Muir, I.J. (1994) X-ray photoelectron spectroscopic study of a pristine pyrite surface reacted with water vapor and air. Geochimica et Cosmochimica Acta, 58, 4667–4679.

Nimick, D.A., and Moore, J.N. (1994) Stratigraphy and chemistry of sulfidic flood-plain sediments in the Upper Clark Fork Valley, Montana. In American Chemical Society Symposium Series, 550, 276–288.

Ohsawa, A., Yamamoto, H., and Watanabe, H. (1974) XPS of valence electrons in FeS_2, CoS_2 and NiS_2. Journal of the Physical Society of Japan, 37, 568.

Parkinson, B. (1990) Layer by layer nanometer scale etching of two-dimensional substrates using the scanning tunneling microscope. Journal of the American Chemical Society, 112, 7498–7502.

Pratt, A.R., Muir, I.J., and Nesbitt, H.W. (1994) X-ray photoelectron and Auger electron spectroscopic studies of pyrrhotite and mechanism of air oxidation. Geochimica et Cosmochimica Acta, 58, 827–841.

Reedy, B.J., Beattie, J.K., and Lowson, R. (1991) A vibrational spectroscopic ^{18}O tracer study of pyrite oxidation. Geochimica et Cosmochimica Acta, 55, 1609–1614.

Rimstidt, J.D., and Newcomb, W.D. (1993) Measurement and analysis of rate data: The rate of reaction of ferric iron with pyrite. Geochimica et Cosmochimica Acta, 57, 1919–1934.

Sasaki, K. (1994) Effect of grinding on the rate of oxidation of pyrite by oxygen in acid solutions. Geochimica et Cosmochimica Acta, 58, 4649–4655.

Sawyer, D.T. (1991) Oxygen chemistry, 223 p. Oxford University Press, New York.

Seah, M.P., and Dench, W.A. (1979) Quantitative electron spectroscopy of surfaces: A standard data base for electron mean free paths in solids. Surface and Interfacial Analysis, 1, 2–11.

Shuey, R.T. (1975) Semiconducting ore minerals, 415 p. Elsevier Scientific, Amsterdam.

Singer, P.C., and Stumm, W. (1970) Acidic mine drainage: The rate-determining step. Science, 167, 1121–1123.

Stumm, W., and Sulzberger, B. (1992) The cycling of iron in natural environments: Considerations based on laboratory results of heterogeneous redox processes. Geochimica et Cosmochimica Acta, 56, 3233–3257.

Stumm, W., and Morgan, J.J. (1996) Aquatic chemistry (3rd edition), 1022 p. Wiley Interscience, New York.

Sutin, N. (1983) Theory of electron transfer reactions: Insights and hindsights. Progress in Inorganic Chemistry, 30, 441–498.

Taylor, B.E., Wheeler, M.C., and Nordstrom, D.K. (1984a) Isotope composition of sulphate in acid mine drainage as measure of bacterial oxidation. Nature, 308, 538–541.

——— (1984b) Stable isotope geochemistry of acid mine drainage: Experimental oxidation of pyrite. Geochimica et Cosmochimica Acta, 48, 2669–2678.

Van der Heide, H., Hemmel, R., van Bruggen, C.F., and Haas, C. (1980) X-ray photoelectron spectra of 3d transition metal pyrites. Journal of Solid State Chemistry, 33, 17–25.

Wehrli, B. (1989) Monte Carlo simulations of surface morphologies during mineral dissolution. Journal of Colloid and Interface Science, 132, 230–242.

——— (1990) Redox reactions of metal ions at mineral surfaces. In W. Stumm, Ed., Aquatic chemical kinetics, p. 311–336. Wiley, New York.

Wei, D., and Osseo-Asare, K. (1995) Pyrite dissolution in aqueous systems: Insights from semiconductor electrochemistry (abs.). Goldschmidt Conference Proceedings, p. 96.

Williamson, M.A., and Rimstidt, J.D. (1994) The kinetics and electrochemical rate-determining step of aqueous pyrite oxidation. Geochimica et Cosmochimica Acta, 58, 5443–5454.

Manuscript received April 28, 1995
Manuscript accepted May 1, 1996

Appendix

Marcus theory has been used for more than three decades to model elementary, outer-sphere electron-transfer (ET) rates. Marcus theory can be extended to electron transfer in bonded systems (e.g., between surface sites) if the donor and acceptor states are not involved in bonding. This criterion is reasonable for Fe 3d orbitals affected by ligand field effects but not involved in primary bonding. The Arrhenius equation gives the rate constant k_{rate} as a function of the activation energy E_a: $k_{rate} = A \exp[-E_a/RT]$. The frequency factor A can be taken as the encounter or collision frequency κ_c times the ET transfer coefficient κ_{el}. The ΔG of activation is expressed in Marcus theory as

$$\Delta G^* = \frac{(\Delta G^\circ_{et} + \lambda)^2}{4\lambda}$$

where ΔG°_{et} is the standard free energy of the reaction and λ is the energy of atomic reorganization about the donor and acceptor atoms. For example, because Fe^{2+}-O bond lengths are different from Fe^{3+}-O bond lengths, significant energy is involved in electron exchange, both in reorganizing the immediate coordination sphere and in reorganizing solvent structure around the aqueous complexes. Note that ΔG°_{et} does not include the energy necessary to form an encounter complex, which can be significant especially if the reacting species are charged.

The reorganization energy λ can be estimated from a knowledge of self-exchange kinetics. Consider the ET reaction between acceptor (A) and donor (D) molecules: $A + D \rightarrow A^- + D^+$. For this ET couple, the rate constants and activation energies of self-exchange come from the reactions $A + A^- = A^- + A$ and $D + D^+ = D^+ + D$. An example is self-exchange between Fe^{2+} and Fe^{3+} in aqueous solution. Because $\Delta G^\circ_{et} = 0$ in the self-exchange reactions, ΔG^* is entirely due to λ. With

$$k_{se} = \nu_{0,se} \exp[\lambda_{se}/4kT] \qquad \text{(A-1)}$$

for self-exchange rate constants, and $\lambda_{AD} = (\lambda_{AA} + \lambda_{DD})/$

2, Marcus theory expresses the rate constant for the desired ET reaction as

$$k_{AD} \approx (k_{AA}k_{DD}k_{AD}f)^{1/2} \quad \text{(A-2)}$$

$$\log f = \frac{(\log K_{AD})^2}{4 \log(k_{AA}k_{DD}/\nu_0^2)} \quad \text{(A-3)}$$

where ν_0 is the root-square average of the frequency factors from the self-exchange reactions. The theory outlined above can be extended to heterogeneous ET reactions at electrode surfaces (Marcus 1965). For ET from an oxide CB to O_2, the Marcus (1965) expression has been simplified by assuming that λ for the electrons leaving the donor of the solid is negligible in comparison with that of the acceptor molecule, $\lambda_A \approx \lambda_{total} = \lambda$ (Kesselmann et al. 1994):

$$k_{ET,het} = \nu_n(r_e)^3\delta \exp\left[\frac{-(\lambda + \Delta G^{o\prime})^2}{4kT\lambda}\right] \quad \text{(A-4)}$$

in which ν_n is the attempt frequency, r_e is the effective radius of the electron in the semiconductor, δ = the effective electron-transfer distance, and $\Delta G^{o\prime}$ is the overall thermodynamic driving force ($\Delta G^{o\prime} = E_{sfc} - E^{o\prime}$, where E_{sfc} is the energy level of the electronic donor state at the surface and $E^{o\prime}$ is the reduction potential of the acceptor molecule). The $(r_e)^3\delta$ term and the exponential term correspond to the κ_{el} and κ_n terms in Equation 11. Prior uses of Equation A-4 to calculate electron-transfer rates from the conduction band of TiO_2 to aqueous O_2 (Gerischer 1991; Gerischer and Heller 1991, 1992; Kesselmann et al. 1994) have assumed $\nu_n = 10^{12}$ s^{-1} to 10^{13} s^{-1}, $r_e = 10^{-9}$ m, $\delta = 3 \times 10^{-10}$ m, and $\lambda = 1.0$ eV.